Identification & State Estimation for Lithium-ion Batteries

Hysteresis & Online OCV Estimation for NMC/Si-C Cells

M. R. Menken

Master of Science Thesis

TU Delft Delft University of Technology

Delft Center for Systems and Control

Identification & State Estimation for Lithium-ion Batteries

Hysteresis & Online OCV Estimation for NMC/Si-C Cells

Master of Science Thesis

For the degree of Master of Science in Systems and Control at Delft University of Technology

M. R. Menken

August 23, 2023

Faculty of Mechanical, Maritime and Materials Engineering (3mE) · Delft University of Technology





Copyright © Delft Center for Systems and Control (DCSC)
All rights reserved.

Delft University of Technology
Department of
Delft Center for Systems and Control (dcsc)

The undersigned hereby certify that they have read and recommend to the Faculty of Mechanical, Maritime and Materials Engineering (3mE) for acceptance a thesis entitled

Identification & State Estimation for Lithium-ion Batteries

by

M. R. Menken

in partial fulfillment of the requirements for the degree of

Master of Science Systems and Control

Dated: August 23, 2023

Supervisor(s):

dr. ir. R. M. G. Ferrari

ir. T. K. Desai

Reader(s):

dr. R. D. McAllister

Abstract

Lithium-ion batteries are the dominant electrochemical energy storage device and are a key enabler of portable electronics and electric vehicles. However, the technology is often criticized for its use of rare metals. Extending the lifetime of lithium-ion batteries can allow for more time to develop rare metal recycling efforts but this requires accurate knowledge of the battery's state-of-health.

The state-of-health is affected by degradation mechanisms that cause a fade in capacity and power over time, which eventually leads to end-of-life. A common way to track capacity fade is to compare state-of-charge values with changes in charge across a time period. The change in charge can be found by accumulating current, while state-of-charge can be tracked using estimation frameworks that use equivalent circuit models to mirror battery behavior. These models require a relationship between state-of-charge and open-circuit voltage to link the cell's internal state with the observed voltage. However, establishing this relationship is a time-consuming process.

Furthermore, the battery voltage partly depends on the direction of current, i.e. whether the battery is being charged or discharged. This hysteresis effect is highly nonlinear and persists when no current is applied. In past lithium-ion cell chemistries, voltage hysteresis was often neglected but recent developments have introduced silicon doping, which improves energy density, leading to a higher range for electric vehicles, but also increases the magnitude of the hysteresis effect. This degrades the accuracy of model-based estimation frameworks that neglect hysteresis. To improve state-of-charge estimation accuracy for silicon-doped cells, battery models can be extended with additional complexity to match the effect of hysteresis and improve the accuracy of state estimates.

This work combines the Plett hysteresis model with a single RC-pair equivalent circuit, the RC-H model, and uses a joint unscented Kalman filter to identify model parameters and estimate the state-of-charge during different dynamic testing profiles performed on an NMC/Si-C lithium-ion battery. A second version of the model replaces the predetermined OCV function with a simplification of the SOC-OCV relationship that is adaptively estimated using the Kalman filter, the A-RC-H model. Both models are benchmarked against a single RC-pair model, with a predetermined SOC-OCV relationship and no hysteresis component.

The results show that the RC-H model produces lower SOC errors, but comes at the cost of additional complexity and lower robustness to initial SOC error. While the A-RC-H model produces reasonable SOC estimations and can reconstruct the main OCV trend, the RMSE and MAE are only close to the RC model when the initial SOC error is small.

Future work could be aimed at understanding typical initial SOC errors and uncertainties in practical scenarios, improving the filter tuning by adapting noise covariances online, and reducing computational cost by separating states and parameters into two filters running at different frequencies. Furthermore, the different frameworks should be combined with capacity estimation methods to confirm the hypothesis that higher SOC accuracy leads to improved estimation accuracy of the total capacity.

Table of Contents

Acknowledgements vii

1 Introduction 1

2 Electrochemistry 5

2-1 Working Principle . . . 5

2-1-1 Electrochemical cells . . . 5

2-1-2 Lithium-ion cells . . . 6

2-2 Electrode Materials . . . 8

2-2-1 Positive electrode . . . 8

2-2-2 Negative electrode . . . 9

2-3 Electrolyte and Separator Materials . . . 9

3 Degradation Mechanisms 11

3-1 Surface Reactions . . . 12

3-1-1 Negative electrode . . . 12

3-1-2 Positive electrode . . . 13

3-2 Active Material Degradation . . . 14

3-2-1 Negative electrode . . . 14

3-2-2 Positive electrode . . . 14

3-3 Composite Electrode Degradation . . . 14

4 Modeling 17

4-1 Equivalent Circuit Model . . . 18

4-1-1 RC circuit . . . 18

4-1-2 Circuit analysis . . . 20

4-1-3 Discretization . . . 21

4-2 Coulomb Counting . . . 22

4-2-1 State-of-charge . . . 23
4-2-2 Capacity . . . 23
4-2-3 Coulombic efficiency . . . 24
4-3 SOC-OCV Relationship . . . 25
4-3-1 Experiment design . . . 25
4-3-2 Voltage hysteresis . . . 26
4-3-3 Ordinary least squares . . . 27
4-4 Hysteresis Model . . . 28
4-4-1 Instantaneous hysteresis . . . 28
4-4-2 Dynamic hysteresis . . . 29

5 Identification & State Estimation **31**
5-1 Unscented Kalman Filter . . . 31
5-1-1 Sigma points . . . 32
5-1-2 Overview . . . 32
5-1-3 Prediction . . . 33
5-1-4 Correction . . . 35
5-2 Identification & State Estimation Framework . . . 36
5-2-1 RC model . . . 36
5-2-2 RC-Hysteresis model . . . 37
5-2-3 Adaptive-RC-Hysteresis model . . . 38
5-2-4 SOC initialization . . . 39

6 Results **41**
6-1 SOC-OCV Relationship . . . 41
6-1-1 Data analysis . . . 42
6-1-2 Function fitting . . . 43
6-1-3 Aging effects . . . 45
6-2 Dynamic Profiles . . . 48
6-3 Filter Tuning Strategy . . . 49
6-4 RC Model . . . 50
6-4-1 Dynamic stress test . . . 50
6-4-2 Driving cycle test . . . 52
6-5 RC-Hysteresis Model . . . 55
6-5-1 Dynamic stress test . . . 55
6-5-2 Driving cycle test . . . 57
6-6 Adaptive-RC-Hysteresis Model . . . 61
6-6-1 Dynamic stress test . . . 62
6-6-2 Driving cycle test . . . 63
6-7 Analysis of the Results . . . 65
6-7-1 Dynamic stress test . . . 65

6-7-2 Driving cycle test 65
6-8 Aging Effects 68
6-8-1 Ohmic resistance 68
6-8-2 SOC estimation 68
6-8-3 Analysis 69

7 Conclusion **73**
7-1 Discussion 74
7-2 Recommendations 74

Bibliography **77**

List of Abbreviations **81**

Acknowledgements

This thesis is the culmination of years of long days and late nights. I am happy to be at the end of it.

I would like to extend my gratitude to my supervisors, Tushar Desai and Riccardo Ferrari, for their wisdom, advice, and patience over the last few months.

Lastly, I want to thank my girlfriend, my friends, and my family for their unwavering support during my years at TU Delft.

Delft, University of Technology
August 23, 2023

M. R. Menken

Chapter 1

Introduction

Over 30 years since the rechargeable lithium-ion battery was made commercially available by Sony, the technology has become indispensable in our everyday lives and is the dominant energy storage device for portable electronics and electric vehicles due to its high energy density, high power density, fast recharge rate, long cycle life, and low discharge rate [1, 2].

Technological innovations and the continued growth of the electric vehicle (EV) market have significantly reduced the cost of Li^+ batteries by about 97% since the 1990s, and the price is expected to drop further as the EV market matures. Li^+ batteries are also likely to play a role in future electricity grids by acting as a storage medium to support unpredictable renewable energy sources [3, 4].

Due to its contribution to sustainable transportation, lithium-ion batteries also have to be as sustainable and safe as possible. Safety concerns are mainly focused on toxicity and flammability. Lithium and cobalt, a common battery material, can be toxic to humans. Especially the production of cobalt metal is known to pollute water sources of human settlements near extraction sites due to ore washing [3]. Relative to other technologies though, the toxicity of lithium-ion batteries is low [1].

Flammability is the biggest concern in Li^+ batteries, as faulty cells are known to catch fire or even explode due to a self-heating process, called the thermal runaway effect. Once activated, the increased heat generation can cause adjacent previously healthy cells to enter into a thermal runaway as well, allowing it to spread through the entire battery pack. The effect is generally caused by overcharging and cell aging, and optimizing cell chemistry to mitigate thermal runaway is an active field of study [5, 6].

The sustainability of lithium-ion batteries is often criticized due to the reliance on two scarce materials, lithium and cobalt. Especially the use of cobalt is concerning as its scarcity is currently classified as 'critical'. Cobalt is actually more abundant than lithium, but most cobalt is extracted as a byproduct of nickel and copper mining, and over 50% of the global cobalt extraction is done in the Democratic Republic of the Congo, a country with a history of political instability, low safety standards, and child labor. This byproduct mining makes cobalt production inflexible and difficult to scale up, while mining cobalt as a primary product

is often blocked by environmental concerns. The strained supply of cobalt is expected to lead to a bottleneck in the production of lithium-ion batteries sometime in the future. Mitigation of this coming bottleneck should thus be a priority if the current growth in Li^+ battery use is to be sustained [3, 7].

The bottleneck problem can be approached on two fronts: more reliance on cobalt-less and cobalt-poor Li^+ chemistries, and scaling-up battery reuse and recycling efforts. Cobalt-less chemistries exist but typically have a lower energy density, which limits their applications to short-range EVs, while cobalt-poor chemistries have become popular in the form of ternary metal oxide materials, where the fraction of cobalt is reduced and replaced by other less scarce metals like manganese and nickel [3].

The disposal of end-of-life batteries requires special handling to avoid toxic materials from adversely affecting the environment and to minimize the risk of fires starting or accelerating due to the presence of flammable battery materials. From a sustainability point of view, recycling lithium-ion batteries is preferred over disposal, but Li^+ battery recycling techniques are mostly intensive processes and expensive, while the current technology for low-cost methods is immature [8].

As an intermediate step between end-of-life and recycling, lithium-ion batteries can be reused instead of disposed of. Reuse can be divided into remanufacturing and repurposing. In remanufacturing, battery packs are partially repaired by finding and replacing the set of batteries that are limiting performance. While repurposing refers to giving the battery a second life in a less-demanding load environment such as in energy storage systems [8].

The desire to reuse and recycle aged batteries highlights the need for methods to determine battery healthiness during both primary and secondary life applications. Battery aging is caused by side reactions inside the cell structure that over time leads to a decrease in charge capacity and an increase in resistance [9].

Health can be determined using experimental methods, but this is often impractical in real-life applications. Instead, dynamical models of lithium-ion batteries, based on equivalent circuits, are used to estimate necessary hidden states, like state-of-charge (SOC) and state-of-health (SOH).

The models require a relationship between the SOC and the open-circuit voltage (OCV), the cell voltage when no load is connected, which is often determined with time-consuming experiments using expensive equipment [1]. Cell aging also causes this SOC-OCV relationship to drift over time, increasing state estimation errors.

These equivalent circuit models are simplified representations and often neglect nonlinear effects, such as hysteresis in the terminal voltage [9]. Neglecting hysteresis is a reasonable assumption in Li^+ cells with purely graphite anodes. However, a recent development in Li^+ cell chemistry is to apply silicon doping to graphite anodes, which improves energy density but also increases voltage hysteresis, resulting in larger state estimation errors [10, 11]. A reduced SOC accuracy also impacts the SOH estimation, as capacity estimation methods often rely on SOC estimations [9, 12, 13].

The uncertainty in the SOC-OCV relationship and the increased hysteresis in silicon-doped graphite cells have motivated the following research questions:

- How can voltage hysteresis be modeled and included in state estimation frameworks for lithium-ion cells with silicon-doped anodes?

- Is the significance of voltage hysteresis in silicon-doped lithium-ion cells sufficient that it is worth the additional complexity of including it in state estimation frameworks?
- Can time-consuming OCV tests be replaced by estimating the SOC-OCV relationship online?

This report begins with two background chapters on the working principle behind lithium-ion battery cells and commonly used materials, in Chapter 2, and the general causes and effects of degradation mechanisms inside the cell, in Chapter 3.

Chapter 4 defines and derives the building blocks for modeling of observed behavior in Li^+ cells, which is followed up by an introduction to the joint unscented Kalman filter in Chapter 5, a model-based observer that combines voltage and current measurements with a battery model to obtain estimates of states and parameters.

Chapter 6 displays and discusses the results of the application of the Kalman filter framework on an NMC/Si-C lithium-ion battery from the publicly available EVERLASTING project data set [14]. The report ends with a conclusion, a discussion, and recommendations based on these results, in Chapter 7.

Chapter 2

Electrochemistry

Electrochemical batteries are energy storage devices that are capable of releasing their stored charge when connected to an electrical circuit. Batteries can be divided into two types: primary and secondary batteries. Primary batteries are non-rechargeable after use, but secondary batteries can reverse the electrochemical reaction when connected to an external power supply, making them rechargeable.

This chapter discusses the working principle of electrochemical cells and how these apply to lithium-ion cell technology. Afterward, the versatility of lithium-ion cells is highlighted by discussing the different electrode and electrolyte chemistries. While many principles are applicable to primary batteries as well, the focus is on secondary/rechargeable batteries.

2-1 Working Principle

The working principle of a lithium-ion battery can be explained by looking at the chemical reactions in the electrochemical cell. The cell can be divided into four parts: the electrodes, the electrolyte, the separator, and the current collectors [1].

2-1-1 Electrochemical cells

The electrodes are the main components in the electrochemical cell, which are materials capable of receiving and releasing electrons and ions. When two electrodes are connected, a natural potential difference, called the electromotive force or open-circuit potential, pressures electrons and ions to move from one electrode, the anode, to the other electrode, the cathode. This discharges the cell. The process of releasing electrons increases the charge of the anode and is called oxidation. At the cathode, the opposite happens and the extra electrons decrease the charge of the cathode, called reduction. This reduction-oxidation (redox) reaction is the driving force behind the electrochemical cell [1].

The natural potential can be overcome by applying a larger potential in the opposite direction. This forces the reaction to reverse. Electrons and cations now move back, charging the cell.

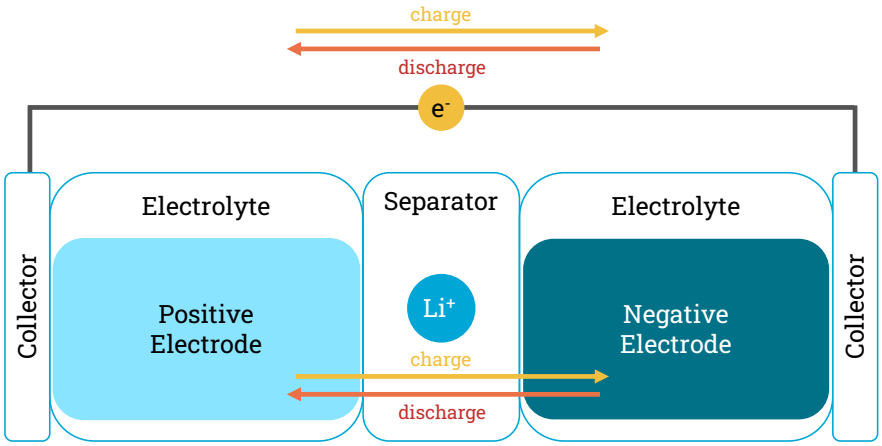

Figure 2-1: Schematic overview of a lithium-ion electrochemical cell.

The terminology also reverses. The anode now becomes the cathode and the cathode becomes the anode. To avoid confusion, the electrodes are instead defined as the positive electrode and the negative electrode. The negative electrode acts as the anode during discharge and the positive electrode is the cathode during discharge [1].

In order to sustain the redox reaction and extract or store energy, the electrons are separated from the electrodes by an external circuit, facilitated by current collectors at both electrodes. While the ions are conducted through the electrolyte, a liquid or solid-like material that surrounds both electrodes that are specialized to conduct ions. The cell is completed by placing a physical barrier between the positive and negative electrode, the separator, which acts as an insulating layer for electrons while allowing ions to pass through. The insulation prevents electrons from directly moving between electrodes, instead of over the external circuit, which would cause an internal circuit to form inside the cell, effectively short-circuiting the cell [1]. The cell can be used to store or extract energy by connecting the external circuit to a power supply or load.

2-1-2 Lithium-ion cells

The principles of a general electrochemical cell also apply to a lithium-ion cell but with some additional complexity. Li^+ cells are insertion-electrode cells, where the electrodes are designed such that lithium ions and electrons can insert themselves into their molecular structure. Before entering the molecular structure lithium-ions react with free electrons in the reaction $Li^+ + e^- \rightarrow Li$. The now charge-neutral lithium atoms intercalate into the electrode material, where they can move freely and diffuse across the electrode's molecular structure [1].

When the voltage potential is reversed the lithium moves towards the surface of the electrode and deintercalates out of the structure. The lithium then releases the electron from its outer valence band, according to $Li \rightarrow Li^+ + e^-$. The lithium ion is conducted to the other electrode through the electrolyte and the separator, while the electrons are collected in the current collectors and travel to the other electrode via the external circuit [1]. A schematic overview of a lithium-ion cell is shown in Figure 2-1, showing the connections between the cell

components and the movement of electrons and lithium-ions between the electrodes during charge and discharge.

The movement of lithium ions in the cell causes lithium concentrations in the electrodes to change over time. The fraction of lithium ions at the negative electrode indicates how much charge is left to discharge from the cell. The relative concentration of lithium at time step k at the negative electrode, $\rho[k]$, is defined as [9]

$$\rho[k] = \frac{c_{avg}[k]}{c_{max}} \tag{2-1}$$

Where $c_{avg}[k]$ is the average concentration at time step k and c_{max} is the maximum possible concentration of lithium ions in the negative electrode. In practice, the charge is not constrained by the maximum concentration, but by upper and lower voltage limits that are based on the cell chemistry. A more intuitive definition for the charge level is then given by

$$z[k] = \frac{\rho[k] - \rho_{0\%}}{\rho_{100\%} - \rho_{0\%}} \tag{2-2}$$

Here, $z[k]$ is the state-of-charge (SOC) at time index k, $0 \leq z \leq 1$. The cell is fully charged when the SOC is 100% and fully depleted at an SOC of 0%. $\rho_{0\%}$ and $\rho_{100\%}$ are the average concentrations of lithium at 0% and 100% SOC. Where 0% and 100% SOC are defined according to the lower and upper voltage limits, respectively. Lithium concentrations are impractical to assess during cell operation, so the SOC is not typically determined using Equation 2-2. Practical methods to determine state-of-charge are discussed in Chapter 4.

Lithium-ion batteries have several advantages that make them the best choice over other battery chemistries in many applications. Li^+ cells can operate at higher voltages than other secondary batteries, typically $V_{avg} = 3.7$ V, which directly correlates to greater energy densities [1]. The chemistry also allows for high power density, long cycle life, and high coulombic and energy efficiency. Lithium-ion batteries are relatively lightweight and have low self-discharge rates compared to other chemistries [15].

However, lithium-ion batteries are not without disadvantages. Even though costs have come down immensely, Li^+ batteries are still relatively expensive due to their use of scarce materials in the electrodes. They are sensitive to overcharging, which means they require additional battery protection circuits that further increase cost [15]. Lithium and, a common electrode material, cobalt are toxic to humans in large doses [16, 17]. This toxicity could be of concern when end-of-life batteries are disposed of incorrectly and in large quantities, which can contaminate the environment [16]. However, relative to other chemistries, the overall toxicity of Li^+ batteries is low [1].

The biggest disadvantage of Li^+ cells is the poor stability at high temperatures and the thermal runaway effect. High cell temperatures cause exothermic reactions between the electrodes and the electrolyte. When the produced heat cannot be dissipated fast enough, the thermal runaway effect occurs. Cell temperature increases, which accelerates the exothermic reaction, further increasing the temperature. This positive feedback loop can trigger fires and explosions in the cell, which can spread to other cells in a battery pack. The major causes are high operating temperatures and short circuits in the cell, caused by manufacturing defects or degradation mechanisms [5].

2-2 Electrode Materials

The previous section discussed the general working principle of lithium-ion cell chemistry. In practice, many different types of chemistries exist that use different materials for the electrodes and the electrolyte. The various types of positive and negative electrodes are mainly of interest here, due to their impact on the energy and power density of a lithium-ion battery.

Chemically, the energy density of a lithium-ion cell can be related to the amount of lithium that can be stored in the electrodes per unit volume and to the difference between the positive electrode potential and the negative electrode potential [9]. A high energy density is often desired, because it allows the battery to power any device for a longer period of time, before requiring charging [1]. For electric vehicles, this means larger distances can be traveled before recharging. Power density is related to the speed at which electrodes can be (de)lithiated. High power densities are desired, because this allows for quicker charging times and a higher amount of energy that can be delivered to a load per time unit.

Choosing between the electrode materials is typically a trade-off between energy density, power density, and cycle life.

2-2-1 Positive electrode

First discovered by Goodenough et al., one of the first Li^+ battery cells was created using lithium cobalt oxide (LCO) as the positive electrode material. Over 30 years since its commercialization, LCO is still widely used as a positive electrode material in Li^+ batteries today [18]. LCO cells are known for their high theoretical specific and volumetric capacity but suffer from high cost and poor thermal stability, which has prevented their application in electric vehicles [18]. The high cobalt content in LCO cells is also not considered sustainable, since the metal is a scarce material [19].

Following the discovery of the LCO electrode, Goodenough et al. later proposed lithium manganese oxide (LMO) electrodes. LMO electrodes do not rely on cobalt metal, which makes them more sustainable, but it suffers from high degradation and a relatively low specific capacity [20, 18]. LMO cells do boast high power density and low cell resistance, which makes them interesting in applications where power capability is preferred over high energy density [1].

Another alternative positive electrode material is lithium iron phosphate (LFP). The main advantage of LFP cells is that iron and phosphate are abundant materials, which makes LFP a cost-effective and sustainable electrode material. The LFP electrode is also known for its high stability. It suffers from a low energy density, which limits the use of LFPs to applications where high safety is preferred over high capacity [1, 18].

LMO and LFP electrodes are improvements on the initial LCO electrode in the areas of safety, cost, and sustainability, but in doing so they lose specific capacity. The current state-of-the-art in high-capacity batteries is a family of electrodes called ternary metal oxides, which combine several metals in one electrode. Nickel manganese cobalt oxide (NMC) and nickel cobalt aluminum oxide (NCA) are part of this family [1, 18]. The ternary metal oxides improve the thermal instability of LCO electrodes while achieving similar or higher specific capacities. In

the NMC electrode, the addition of manganese allows for higher structural stability while nickel increases the specific capacity. Some fraction of cobalt is still required to avoid nickel from occupying positions meant for lithium, which has a negative effect on the reversibility of the reaction [18]. The NCA electrode replaces manganese with aluminum, lowering costs. Ternary metal oxides thus improve upon the original LCO electrode and lower the fraction of cobalt in the electrode, which improves sustainability. Ternary metal oxides are currently popular in electric vehicle applications due to their high energy density and stability [18].

2-2-2 Negative electrode

Initial research into Li^+ cell used lithium metal as the negative electrode, which carried significant safety risks due to the high reactivity of lithium [18]. The problem was largely solved by Yoshino et al. by replacing lithium metal with a carbonaceous material, which allows for a much more stable and safe (de)intercalation process. This would eventually evolve into using the carbonaceous material graphite, which is the dominant negative electrode material in present-day batteries [18, 21]. Relative to a metal-oxide positive electrode, graphite has a low electrode potential, which results in a high cell voltage because the overall voltage is determined by the difference between the positive and negative electrode potentials. Graphite is well-balanced compared to other negative electrode materials, having low cost, high power density, and long cycle life [21]. Graphite is also sustainable, as its only chemical component is carbon. Graphite electrodes are built from stacked graphene layers with hexagonal structures. When lithiated, lithium atoms occupy and move around the spaces between graphene layers. Variations of graphite anodes exist, where the main difference is the uniformity of the graphene layers in the overall structure of the graphite [1].

Graphite is not the only negative electrode material in use. Lithium titanate oxide (LTO) cells use titanate oxide in their negative electrode, which allows for much faster charging and power delivery than graphite and maintains a long cycle life. The disadvantage of LTO cells is that cell voltages are severely reduced compared to graphite, which correlates to a lower energy density [1]. LTO cells are interesting in applications where power density is preferred over energy density, e.g. short-range EVs and renewable energy storage [22, 23].

Another alternative to graphite is silicon. Silicon is able to store more lithium per unit volume in its chemical structure than graphite, which greatly boosts the cell's energy density. The major disadvantage when using silicon anodes is that the cycle life is heavily reduced [1, 21]. The large lithium capacity of silicon causes its molecular structure to heavily increase in volume when lithiated compared to its unlithiated state. When cycled, the repeated large changes in volume quickly cause irreversible damage to the silicon structure, which reduces its capacity to hold lithium [18]. A recent trend is to combine the properties of graphite and silicon by doping graphite electrodes with a small amount of silicon. When balanced correctly, the cell's lithium capacity is increased while the cycle life effect is minimized [18, 21].

2-3 Electrolyte and Separator Materials

The electrolyte and the separator are both parts of the battery cell that have to be designed to conduct ions while limiting the movement of electrons. High ionic conductivity contributes directly to increased reversible capacity, power capability, and cycle life [24].

In lithium-ion cells, the electrolyte is often a lithium salt dissolved in an organic solvent material. The solvent does not participate in the chemical reaction but has a small charge polarization that facilitates the ionization of the lithium salt and the conduction of lithium ions across the electrolyte [1].

The separator is a permeable membrane material. The holes in the membrane have to be large enough to allow lithium ions to pass through but small enough to prevent the positive and negative electrodes from contacting and short-circuiting the cell [1, 24]. This property has to be maintained over the entire working temperature range of the cell, meaning the separator requires a high degree of mechanical strength and thermal stability. These safety requirements are at odds with battery performance. Increasing the separator thickness and decreasing the porosity, for example, increases mechanical strength but decreases ionic conductivity [24]. Most Li^+ cell separators are made from microporous polyolefin membranes, which have high mechanical strength but suffer from large thermal shrinkage at high temperatures [24].

Chapter 3

Degradation Mechanisms

The reversibility of the redox reaction in lithium-ion batteries is never ideal due to parasitic side reactions at several locations in the cell and structural deterioration of the electrodes, resulting in irreversible loss of lithium inventory (LLI) and loss of active material (LAM) [25].

The loss of lithium and active material affects the total capacity of the cell, as there are fewer lithium ions to pull electrons from the external circuit and fewer locations for the lithium to be stored. This causes a slow fade in the capacity as the cell ages [9]. The deterioration also reduces electronic and ionic conductivity through the cell components, which is inversely proportional to the cell resistance. This increasing resistance causes a fade in the power that the cell can deliver or receive.

The capacity fade and power fade are the two main factors that determine the overall state-of-health (SOH) of a battery cell. The SOH is quantified by relative relationships between the current values and the begin-of-life (BOL) values, defined as

$$\text{SOH}_C = \frac{C}{C_{BOL}} \qquad \text{SOH}_R = \frac{R}{R_{BOL}}$$

Where SOH_C is the capacity state-of-health, and SOH_R is the resistance state-of-health. The BOL capacity is usually defined as the nominal capacity given by the manufacturer or the initial capacity estimated from a capacity test. Picking an initial resistance value is less straightforward, because of its strong dependence on temperature and SOC [9]. Note that an increase in resistance can also lead to a lower discharge capacity, as the minimum operating voltage is reached earlier due to the higher ohmic losses [26]. Discharge capacity should not be confused with total capacity. The definitions are discussed in more detail in Subsection 4-2-2.

Typical end-of-life (EOL) definitions for electric vehicles are a doubling of the resistance or a 20% capacity fade, i.e. $\text{SOH}_C = 80\%$ and $\text{SOH}_R = 200\%$.

A visual summary of the chapter can be found in Figure 3-1, adapted from [26], which shows the path from cause to effect along different mechanisms and modes inside the lithium-ion cell. Although the degradation mechanisms are complex and often interrelated, they can be

divided into three categories: surface reactions, active material degradation, and composite electrode degradation. These are indicated in the cause and effect map by using different colors, turquoise for surface reactions, gold for active material degradation, and orange for composite electrode degradation.

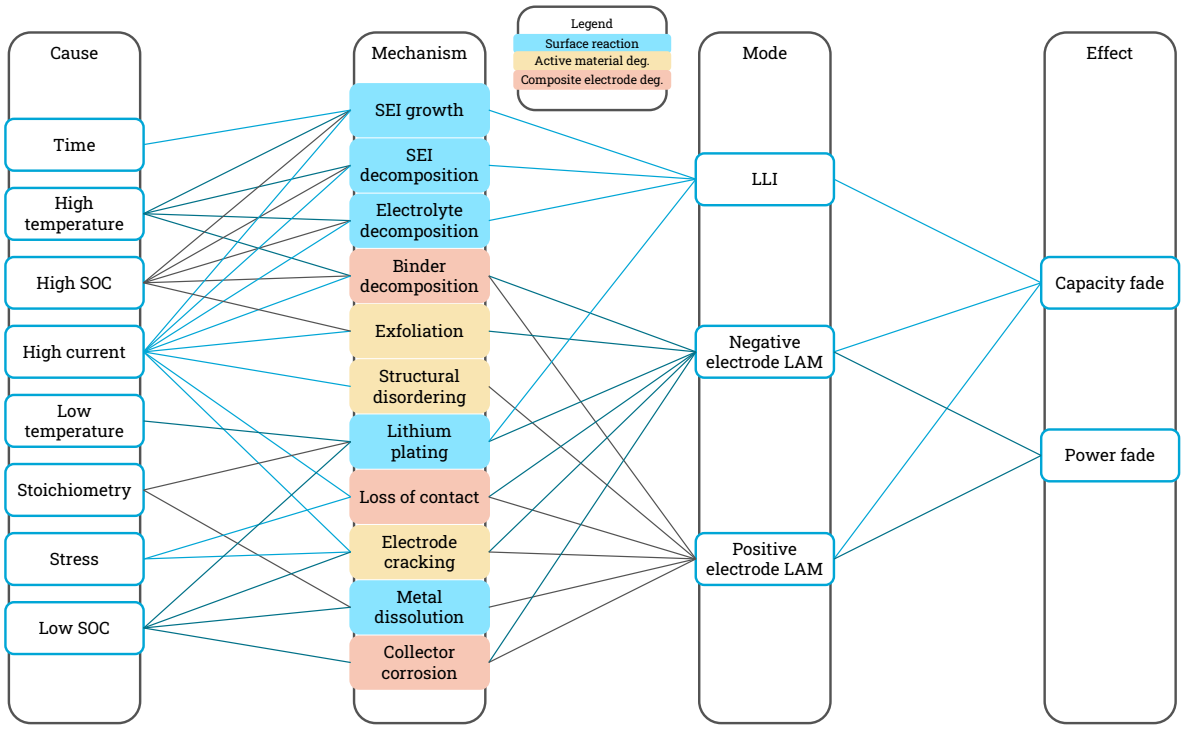

Figure 3-1: Cause and effect map for common lithium-ion cell degradation mechanisms, adapted from [26].

The relative severity of mechanisms depends highly on the exact chemistry of the electrode and the electrolyte. For metal-oxide/graphite cells, the main mechanisms that lead to capacity fade and power fade are typically growth in the SEI layer and material loss [9]. This chapter describes the main causes of LLI and LAM at both the negative and positive electrodes, with a focus on graphite-based negative electrodes.

3-1 Surface Reactions

Over the life span of a lithium-ion cell, the positive and negative electrodes continuously interact with the aqueous electrolyte, which results in thin layers of various chemical compounds on the surface of both electrodes.

3-1-1 Negative electrode

Lithium-ion cells are manufactured in a discharged state, with all lithium inside the positive electrode. After the fabrication process is completed, a cell requires a charge cycle to be

activated, which lithiates the negative electrode for the first time [1]. When lithiating graphite electrodes, the electrode potential drops outside the working region of the electrolyte, resulting in a violent reaction between the organic solvent in the electrolyte and the graphite material [9].

The reaction quickly forms a thin film around the surface of the electrode, which acts as a passivation layer between the electrode and the electrolyte, the solid-electrolyte interphase (SEI). Once fully formed, the SEI layer stops the electrode and electrolyte from interacting directly, which prevents the reaction from completely destroying the electrode and semi-stabilizes the SEI layer formation. The initial formation of the layer is thus actually desired for the safe operation of the cell [1].

However, the formation of the SEI film consumes lithium atoms, leading to irreversible capacity fade, and reduces electronic and ionic conductivity, as the particles have to move through an additional membrane, resulting in increased cell resistance and power fade. After the formation process, the SEI layer continues to grow from side reactions inside the cell at a slow rate, continuously eating up lithium, decreasing cell capacity and increasing cell resistance [27].

SEI layer growth can be further exacerbated by high temperatures and currents. At high SOC, the electrode potential of graphite is lowest, and the difference between the working region of the electrolyte is highest, causing SEI layer growth to be amplified. Under high temperatures, the SEI film breaks down, exposing graphite to the electrolyte and causing another violent SEI layer formation process [9].

High currents can allow for some of the electrolyte solvents to travel with the lithium into the graphite electrode, called co-intercalation. The solvents react with the graphite inside the electrode, cracking parts of the electrode or peeling off entire layers, which is called graphite exfoliation. The surface inside the crack is then exposed to more electrolyte material, which leads to even more SEI layer formation [27].

The electrolyte is often contaminated by trace amounts of water molecules and some electrolyte salts can react with water to form hydrofluoric acid. When it contacts the SEI layer, the acid has a thinning effect, which can expose graphite and cause rapid SEI growth. The acid also reacts with the positive electrode and causes electrode ions to dissolve in the electrolyte. These ions can move through the separator to the negative electrode, where they can form part of the SEI layer and block lithium ions from moving through the SEI, a mechanism called anode poisoning [28].

At cold temperatures, typically below freezing, the diffusion of lithium ions through the negative electrode is slower. When combined with low SOC, the slower diffusion allows lithium ions from the electrolyte and electrons from the external circuit to form lithium metal and stick to the electrode surface, instead of intercalating into the structure. The lithium metal plating enhances SEI layer growth and enables metal dendrites to form. Dendrites increase the self-discharge rate of the cell and can also grow large enough to penetrate the separator membrane and short-circuit the cell [1, 9, 27].

3-1-2 Positive electrode

Reactions between the electrolyte solvents and active electrode material are present at the positive electrode as well. However, here this reaction only plays a small part in the formation

of a film around the electrode. Instead, metal dissolution is generally the primary cause of film formation and growth [27]. This layer is sometimes referred to as the cathode-electrolyte interphase (CEI), as the film is often thinner and the involved mechanisms are different from SEI formation at the negative electrode [25]. Metal dissolution is a loss of active material process, where metals from the electrode ionize and dissolve into the electrolyte. The ions can form chemical compounds and form part of the CEI layer. The ions can also move through the electrolyte, similar to lithium, and interact with the negative electrode on the other side of the separator, causing anode poisoning, as mentioned in the previous subsection [27].

The process is accelerated by the presence of hydrofluoric acid in the electrolyte and tends to occur more at high and low SOC, and at high temperatures [9].

3-2 Active Material Degradation

Degradation in the active material is associated with irreversible alterations in the structure of the electrodes, typically from volume changes after repeated lithiation and delithiation cycles.

3-2-1 Negative electrode

When the negative electrode is lithiated during charge, the intercalation of lithium atoms causes the electrode structure to deform, increasing in volume. Once discharged, the volume generally reverts back to the original size. However, repeated charge-discharge cycles cause cracking in the structure and in the SEI film, which exposes the negative electrode to more electrode-electrolyte reactions. Decreasing capacity and increasing resistance due to rapid SEI layer formation.

3-2-2 Positive electrode

Lithiation and delithiation at the positive electrodes cause volume changes and distortions in the crystal lattice of the electrode. These phase transitions result in large stresses on the structure that lead to the cracking of the electrode particles. The cracks decrease the total amount of lithium that can be stored in the electrode. This degradation typically occurs when overcharging the cell [29].

The electrode particles can also break down completely, called structural disordering, which destroys lithium storage sites and can trap lithium inside the electrode, both leading to capacity fade [9].

3-3 Composite Electrode Degradation

Practical electrodes in lithium-ion cells contain additives and binders to improve electronic conductivity and electrode cohesion but do not take part in the main reactions. The additives can oxidize over time and deformation of the active material during (de)lithiation can cause the binder material to fail, which reduces electronic conductivity between the electrode and

the current collector. Additionally, particles might become fully isolated from the electrode, leading to capacity fade [9].

Another result of deformation is a reduction of electrode porosity. A porous electrode allows for a large surface to be surrounded by the electrolyte. This facilitates the transport of lithium and thus improves ionic conductivity. As deformation from repeated cycling decreases electrode porosity, the ionic conductivity drops and the cell resistance increases [27].

Lastly, over-discharging a battery cell can cause copper from the current collector to corrode and dissolve copper ions into the electrolyte. The copper ions can react with the SEI layer, where they increase cell resistance and enhance the growth of metal dendrites. At the current collector, the contact with the electrode is reduced, increasing cell resistance. The corrosion also causes an inhomogeneous distribution of voltage potential and current due to an uneven resistance, which facilitates lithium plating and accelerates the aging process in some parts of the cell [9].

Chapter 4

Modeling

The process of modeling lithium-ion cell behavior starts by addressing the question of what elements should be included in a cell model. In electric vehicles, an important metric is the current travel range, which allows the end-user to judge whether a destination is reachable or if a battery recharge is needed. The range is proportional to the amount of energy stored in the vehicle's battery pack. On a cell level, the available energy can be determined via [9]

$$E[k] = C \int_{z_{min}}^{z[k]} \text{OCV}(\zeta) d\zeta \tag{4-1}$$

Where $E[k]$ is the available energy at the time index k in Wh, C is the total capacity in Ah, OCV is the open-circuit voltage, and $z[k]$ is the current state-of-charge (SOC). A minimum SOC, z_{min}, is usually set to avoid high degradation effects at low SOC and reserve some energy for emergency use [9]. The open-circuit voltage (OCV) is a measure of the natural cell potential and increases monotonically with increasing SOC.

The available energy is only one part of the picture, however. To ensure the battery is operated both efficiently and inside safety limits, estimates of available charge and discharge power are required. Cell power is correlated with the electrical resistance inside a cell.

The evaluation of the available energy and power thus depends on the estimation of the total capacity, the current SOC, the mapping between the SOC and the OCV, and the cell resistance.

The chapter starts by introducing equivalent circuits that model the voltage behavior of a battery cell to link voltage and current measurements with cell resistance and open-circuit voltage. Afterward, the coulomb counting method for SOC estimation is described and definitions for common terminology are given. Lastly, experiments to uncover the SOC-OCV relationship are discussed and a dynamical model for voltage hysteresis is derived.

4-1 Equivalent Circuit Model

Battery cells are complex electrochemical devices, requiring extensive physics-based models for high-fidelity representation. However, these models are built from partial differential equations, which are generally too computationally complex to be used in real-time systems. Therefore physics-based models are typically used for battery cell simulations, where computational resources are less constraining [30].

Circuit models limit themselves to empirical observations in the electrical domain and largely neglect complex chemical behavior. This results in models with lower fidelity but reduces the computational cost. Equivalent circuit models can be expressed as a set of ordinary differential equations that can easily be combined with filtering or observer frameworks, like Kalman or H_∞ filters, to predict and correct internal states in real-time [31, 32, 33].

4-1-1 RC circuit

Figure 4-1 shows the measured battery voltage response when a step current load is applied to the cell. A dynamical relationship can be observed with the current as the input and the voltage as the output.

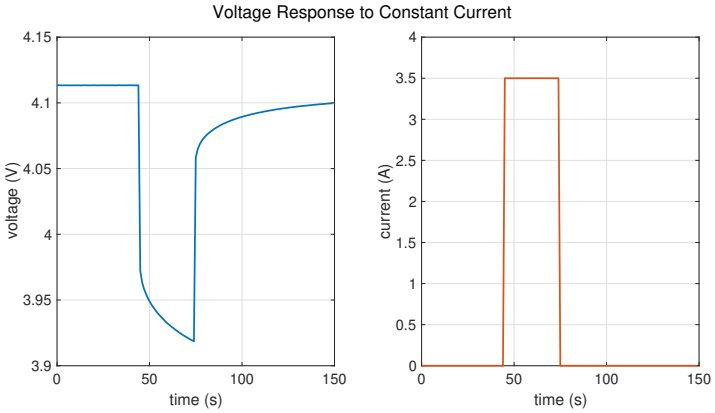

Figure 4-1: Voltage response to constant current [14].

Two distinct phases can be observed in the voltage response. In the first phase, the voltage drops almost instantaneously to a lower level. Using the electrical circuit analogy, this can be associated with a typical voltage drop over an ohmic resistance element. Leading to the first part of the circuit shown in Figure 4-2. Where i is the current going through the cell, R_0 denotes the ohmic resistance, and V_t is the terminal voltage, which is the voltage measured across the battery.

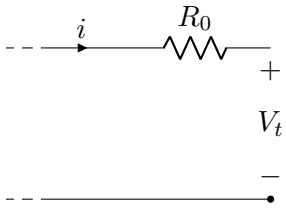

Figure 4-2: Partial equivalent circuit with ohmic resistance.

The second phase in Figure 4-1 shows a slower transient response in the terminal voltage, which is called the polarization phase. This indicates that there are elements inside the cell that are resisting changes in the voltage. Continuing with the circuit analogy, this behavior can be represented by a resistor and capacitor connected in parallel, i.e. an RC-pair. The RC-pair can be combined with the ohmic element to create the next iteration of the equivalent circuit, visualized in Figure 4-3.

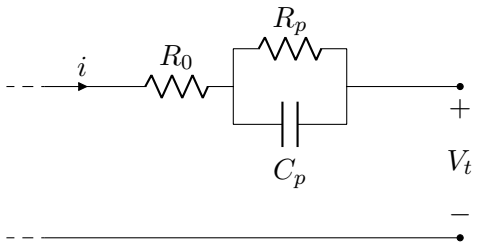

Figure 4-3: Partial circuit with RC-pair and ohmic resistance.

The circuit is completed by adding a voltage source, which represents the inherent voltage potential of the battery cell. Due to voltage losses over the other circuit components, this potential is only directly measurable when zero current is flowing through the battery, which is why this potential is referred to as the open-circuit voltage (OCV). The OCV is not constant. Instead, its value depends on several factors, most notably state-of-charge and temperature. The open-circuit voltage is discussed in more detail in Section 6-1.

The final circuit diagram, with the OCV source included, is shown in Figure 4-4. The circuit is often referred to as the RC or Thevenin circuit because the RC-pair is the distinctive feature that separates it from other equivalent circuits.

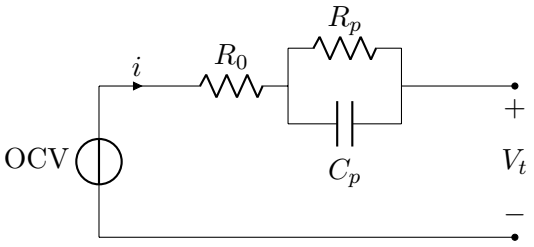

Figure 4-4: Finalized RC circuit.

This is the most basic version of the RC circuit. In general, a single RC-pair cannot completely capture battery behavior, because the transient voltage response is nonlinear. The

nonlinearity can be more accurately modeled by constant phase elements (CPE) which are generalized versions of the typical impedance elements. CPEs are fractional-order elements, which increases the computational complexity of the model. Alternatively, CPEs can be approximated by adding additional RC-pairs in series with each other. In practice, however, a single or double RC-pair often provides sufficient accuracy [31, 32, 33]. In this work, the model is limited to a single RC-pair.

4-1-2 Circuit analysis

According to Kirchhoff's voltage law, the net sum of voltages has to equal zero. Leading to the relationship

$$\text{OCV} = V_t + V_p + V_0$$

Where V_p is the voltage loss across the RC-pair, or polarization voltage for short, and V_0 is the ohmic voltage loss over the ohmic resistance. In practical applications, only the terminal voltage is measurable and the ohmic voltage loss can be expressed in the control variable i and the ohmic resistance R_0 using Ohm's law. The previous equation is then reformulated as

$$V_t = \text{OCV} - V_p - R_0 i \tag{4-2}$$

The circuit can be transformed into a state-space format by analyzing the current flow using electrical laws. According to Kirchhoff's current law, the current flowing through both arms of the RC-pair must sum up to the total current through the circuit, namely

$$i = i_1 + i_2 \tag{4-3}$$

i_1 is the current flowing through R_p and i_2 is the current through C_p. Through the law of capacitance, it is known that i_2 is proportional to the amount of capacitance multiplied by the time derivative of the voltage across the RC-pair, which gives

$$i_2 = C_p \dot{V}_p$$

i_1 can also be related to the RC-pair voltage by using Ohm's law, which states that i_1 is proportional to the voltage divided by the magnitude of the resistance, written as

$$i_1 = \frac{V_p}{R_p}$$

These relationships can be inserted into Equation 4-3, resulting in

$$i = \frac{V_p}{R_p} + C_p \dot{V}_p$$

Rewriting this equation yields a dynamical relationship for the change in polarization voltage with respect to time,

$$\dot{V}_p = -\frac{1}{R_p C_p} V_p + \frac{1}{C_p} i \tag{4-4}$$

Which is an ordinary differential equation. By combining Equation 4-4 with Equation 4-2, the equivalent circuit can be formulated in state-space form as

$$\begin{aligned} \dot{V}_p &= -\frac{1}{R_p C_p} V_p + \frac{1}{C_p} i \\ V_t &= \text{OCV} - V_p - R_0 i \end{aligned} \tag{4-5}$$

Similar to the OCV, the circuit parameters, R_0, R_p, and C_p, are not constant values, but change continuously based on the current chemical structure of the cell. This variance occurs on both short and long timescales and is related to the state-of-charge, temperature, and state-of-health.

4-1-3 Discretization

For digital implementation, the polarization voltage relation from Equation 4-5 is more useful when expressed as a difference equation, which can be found by discretizing the dynamical equation. Any differential equation of the form

$$\dot{x}(t) = Ax(t) + Bu(t) \tag{4-6}$$

can be written with the variation-of-constants-formula, as

$$x(t_{k+1}) = e^{A(t_{k+1}-t_k)} x(t_k) + \int_0^{t_{k+1}1-t_k} e^{As} \mathrm{d}s B u(t_k) \tag{4-7}$$

Where k denotes the discrete-time index. When the sampling time T_s is known, the equation can be rewritten to

$$x(t_{k+1}) = e^{AT_s} x(t_k) + \int_0^{T_s} e^{As} \mathrm{d}s B u(t_k) \tag{4-8}$$

In general, A and B are matrices, and solving the convolution integral is not straightforward. However, for a first-order differential equation A and B are both scalars, denoted by a and b. When a, b, and the input $u(t_k)$ are assumed to be constant during the interval between samples, the convolution integral can be simplified to

$$\int_0^{T_s} e^{as} \mathrm{d}s b u(t_k) = \frac{b}{a} \left(e^{aT_s} - 1 \right) u(t_k)$$

Comparing Equation 4-6 with Equation 4-4, it can be seen that in the polarization voltage equation, a and b are linked to the circuit parameters as

$$a = -\frac{1}{R_p C_p} \qquad\qquad b = \frac{1}{C_p}$$

The discretized equation can be written in the form

$$V_p(t_{k+1}) = e^{-\frac{T_s}{R_p C_p}} V_p(t_k) + R_p \left(1 - e^{-\frac{T_s}{R_p C_p}} \right) i(t_k) \tag{4-9}$$

Lastly, notation is simplified by defining the polarization time constant τ as $\tau = R_p C_p$ and by referring to the time indices with k and $k+1$. Together with Equation 4-2 this results in the following discrete-time state-space of the RC circuit,

$$\begin{aligned} V_p[k+1] &= e^{-T_s/\tau} V_p[k] + R_p \left(1 - e^{-T_s/\tau}\right) i[k] \\ V[k] &= \text{OCV}[k] - V_p[k] - R_0 i[k] \end{aligned} \tag{4-10}$$

4-2 Coulomb Counting

One of the reasons for investigating methods to model lithium-ion batteries is to find a way to track unmeasurable states, like state-of-charge. Equivalent circuit methods greatly simplify battery behavior to a small set of equations, but the model parameters are all time-varying and contain no direct link to state-of-charge. An additional equation is thus needed to track battery SOC. A simple, but effective, method is to count the amount of charge that passes through the battery during a specified interval. The change in charge $\dot{q}$ can then be described by the differential equation

$$\dot{q} = -\eta i \tag{4-11}$$

Where η is the coulombic efficiency, which is defined as 1 during discharging and generally $\leq$1 when charging. i is the current going through the cell. Throughout this work, the current is defined as positive when discharging the battery and negative during charging. Using that definition, a minus sign is required, as the amount of charge increases when charging and decreases during discharging.

During battery operation, it is not intuitive to directly use the charge level as a remaining capacity indicator. Instead, the state-of-charge (SOC) is used, which is a relative definition. The state-of-charge is defined as the charge level relative to the total amount of cell capacity. Normalizing the differential equation then yields

$$\dot{z} = -\frac{1}{3600}\frac{\eta}{C} i \tag{4-12}$$

Where z denotes the SOC and C is the total capacity of the cell. Capacity is often given in milli-ampere-hours (mAh) or ampere-hours (Ah). Here, the capacity is defined in units of Ah, so the capacity has to be multiplied by 3600 to convert to coulombs. To compute the SOC at a time t, the differential equation can be discretized using the forward Euler method, which states

$$z[k+1] = z[k] + T_s \dot{z}[k] \tag{4-13}$$

Resulting in the difference equation

$$z[k+1] = z[k] - \frac{T_s}{3600}\frac{\eta}{C} i[k] \tag{4-14}$$

This equation is widely used as a SOC estimator and is often referred to as the coulomb counting equation [1]. Coulomb counting is a simple SOC estimator but suffers from the following error sources that affect its long-term behavior [34]:

1. Initialization error - Coulomb counting relies on an accurate initial state-of-charge. Any error will result in a constant bias.

2. Measurement noise error - The measured cell current will not be exactly equal to the actual current acting on the battery, leading to an accumulating error due to the integration of noise.

3. Discretization error - Euler discretization is only a first-order approximation of the integration and assumes that the change in state-of-charge is constant during the sampling interval.

4. Parameter error - The total capacity decreases over the lifetime of the cell due to chemical degradation, overestimating the actual SOC, and coulombic efficiency varies slightly with temperature and current [35].

In spite of these disadvantages, coulomb counting is still a valuable tool in state-of-charge estimation and errors can be minimized by adding a second SOC estimator using the open-circuit voltage of the battery.

4-2-1 State-of-charge

Equation 4-14 defines the change in SOC as a fraction relative to the total capacity, but a full understanding of the state-of-charge requires definitions for when the cell is fully charged, at 100% SOC, and when the cell is empty, at 0% SOC.

The SOC is defined to be at 100% when the cell is charged by a completed constant current-constant voltage (CC-CV) profile. The full CC-CV profile first charges the battery with a constant current. Once the maximum voltage is reached, which depends on the cell chemistry and is often set by the manufacturer, the voltage is kept constant and the current tapers off until a specific cut-off current is reached. The charging process then stops and the cell is at 100% SOC [1].

To reach an SOC of 0%, the cell has to be discharged with an (infinitesimally) small current until the minimum voltage, set by the manufacturer, is reached. If the current is too large, ohmic voltage losses inside the cell will cause the minimum voltage to be reached at a higher SOC level [1]. The terminology is connected with the definition of total capacity and will be explained further in the next subsection.

4-2-2 Capacity

Capacity is often loosely defined in the scientific literature, which can be a source of confusion due to the fact that several interpretations are possible depending on the point of view and application.

The first capacity to define is the nominal capacity. This capacity is given by the manufacturer of the battery cell and represents the design capacity of the cell. The real initial capacity will generally deviate from the nominal capacity [12]. Current loads are often given as a relative value to the nominal capacity using C-rates. C-rates reflect the time it will take to charge

or discharge the cell, written as C/t, where t is the number of hours it will take to charge or discharge the cell if the current is kept constant. For example, drawing a C-rate of C/2 from a battery cell with a nominal capacity of 2 Ah means the cell is discharged with 1 ampere, which should take two hours if kept constant and assumes that the total capacity is equal to the nominal capacity.

The nominal capacity should not be confused by the total cell capacity C, used in Equation 4-14, which is defined as the total amount of charge removed from the cell when discharging from 100% SOC to 0% SOC at an infinitesimally small current. With an infinitesimally small current, completely discharging the cell is incredibly time-consuming, so total capacity is often computed using C/20 or C/30 tests. The current during the test is measured and can be summed over the duration of the experiment [1]. The total capacity in Ah can then be found via

$$C = \frac{T_s}{3600} \sum_{k=0}^{N} i[k] \tag{4-15}$$

Where T_s is the sampling time and the division by 3600 is needed for the conversion to Ah. The total capacity is independent of current load and temperature but reduces over time due to degradation phenomena inside the cell [1]. During device or vehicle operation, performing low-current full discharge experiments is impractical. Instead, other methods are employed to estimate capacity. A common method is to express the coulomb counting equation in terms of the total capacity and sum the currents over some window l, which can be written as

$$\left(z[k] - z[k-l]\right) C = \frac{T_s}{3600} \sum_{j=k-l}^{k-1} i[j] \tag{4-16}$$

The total capacity can then be solved online by using recursive least squares techniques [9]. The main difference with Equation 4-15 is that this method requires SOC values. These values cannot be directly estimated by coulomb counting to avoid a circular dependency. Instead, SOC estimations need to come from voltage-based methods or from frameworks combining coulomb counting and voltage-based methods. The accuracy of the total capacity estimation is highly dependent on the accuracy of the SOC estimations. Alternatively, a data-driven approach can be taken, where lookup tables or machine learning models are created to infer total capacity online from voltage, current, and temperature observations. The main downside to these methods is that they require large amounts of high-quality training data [12, 13].

The last capacity definition is the discharge capacity, which is defined as the total amount of charge removed when discharging from 100% SOC until the cut-off voltage is reached. The discharge capacity is always lower than or equal to the total capacity because the cut-off voltage is often reached before 0% SOC due to increased ohmic losses at higher current loads. The discharge capacity is thus dependent on current, but also on temperature because the ohmic resistance varies with temperature. Just as the total capacity, the discharge capacity trends downwards over time [1].

4-2-3 Coulombic efficiency

When keeping track of the amount of charge going into and out of a battery cell over the duration of a battery cycle, it can be observed that the amount of charge going in exceeds the

amount of charge going out. This implies that there are charge losses inside the cell, which is quantified by the coulombic efficiency η, defined as [1]

$$\eta = \frac{\text{charge out}}{\text{charge in}} \tag{4-17}$$

The charge losses are caused by several side reactions inside the Li^+ cell that lead to a degradation in performance over time. The coulombic efficiency can therefore be directly linked to cycle-related cell degradation [35]. An advantage of lithium-ion cells is that their coulombic efficiency is high compared to other battery chemistries, typically ≥ 0.99 [1, 35].

4-3 SOC-OCV Relationship

The stability of the coulomb counting method is problematic due to several error sources. SOC is not a standalone state but has a clear correlation with other battery parameters. One correlation is with the open-circuit voltage (OCV) of the battery cell. The OCV monotonically increases with increasing SOC and is defined as the terminal voltage when no load is applied and the cell has reached thermal equilibrium. This definition makes it difficult to measure in a practical setting and is therefore determined in laboratory testing under isothermal conditions with highly accurate voltage and current sensors.

4-3-1 Experiment design

Two common OCV tests are the low-current test and the incremental-current test [36, 1]. To gather data in the entire working range of the battery cell, both tests discharge the cell from 100% SOC to 0% and then charge the cell from 0% to 100% again.

The incremental test uses a current pulse to discharge a specific amount of SOC, typically 10%. The cell is then rested for a couple of hours to allow it to reach thermal equilibrium. The OCV is assumed to be equal to the measured terminal voltage at the end of the resting period. The current pulse is repeated until 0% SOC. The same test is then done for the charge curve by charging the battery cell with current pulses of equal width [36].

The second method is the low-current test, which discharges the cell from 100% SOC to 0% using a small current value, typically C/20 or C/30 [1]. Voltage losses from polarization and ohmic effects are proportional to the magnitude of the current and by using a low C-rate these losses are considered negligible. After discharging to 0%, the cell is rested such that thermal equilibrium is reached. The same C-rate is then used to charge the battery until the battery reaches 100% again. One advantage of the low-current test is that the data can also be used to estimate the total capacity of the cell, as discussed in Subsection 4-2-2. The EVERLASTING data set used in this work contains low-current tests with a C/20 profile at an ambient temperature of 25°C.

In the low-current test, current sensors keep track of the accumulated charge during the charge and discharge phases. This can be leveraged to compute the SOC at every point in the experiment. First, the depth-of-discharge is defined as the difference between the

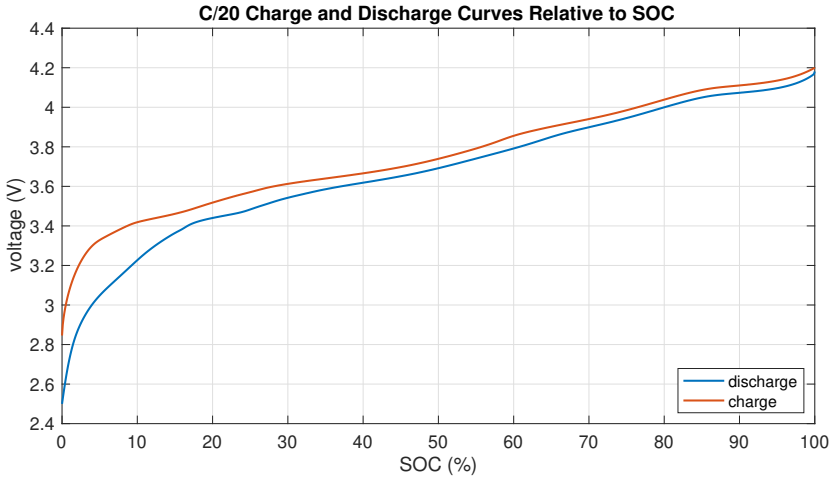

Figure 4-5: C/20 charge and discharge curve relative to SOC.

accumulated charge out of the cell and the accumulated charge into the cell multiplied with the coulombic efficiency, at a time index k [1],

$$\text{DOD}[k] = \text{charge out}[k] - \eta \cdot \text{charge in}[k] \tag{4-18}$$

Where η is computed by dividing the total charge out by the total charge in (Equation 4-17). The SOC at every time index k throughout the experiment can then be calculated as [1]

$$z[k] = 1 - \frac{\text{DOD}[k]}{\text{total charge out}} \tag{4-19}$$

Note that the total charge out is approximately equal to the total capacity. Figure 4-5 shows the SOC-voltage relationship for both charge and discharge after performing a C/20 test under an ambient temperature of 25°C. The data is taken from the EVERLASTING project, which subjected multiple Li^+ battery cells with an NMC positive electrode and a silicon-doped graphite negative electrode (NMC/Si-C) to cell aging tests [14]. This chemistry has a maximum voltage of 4.2 V and a minimum of 2.5 V. More details on the used data set are given in Chapter 6.

4-3-2 Voltage hysteresis

In Figure 4-5 the charge and discharge curves do not overlap. Instead, the charge curve consistently shows a higher voltage than the discharge curve, i.e. the direction of travel changes the SOC-voltage relationship. This phenomenon is common in physics and is referred to as hysteresis [1, 10]. It can also be seen that the voltage hysteresis is not constant but varies with SOC, with higher hysteresis at low SOC.

Several explanations and models of hysteresis have been proposed. The general explanation is that for the same SOC, multiple thermodynamic equilibrium potentials are possible, as two different phases can exist within an active particle, a lithium-rich and lithium-deficient one. The exact composition of these phases is path dependent [37]. Because of the voltage

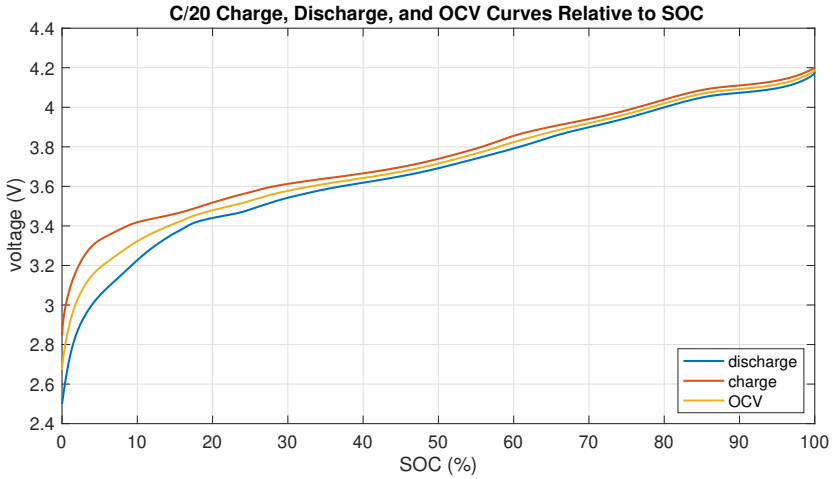

Figure 4-6: C/20 charge, discharge, and OCV curve relative to SOC.

hysteresis, the SOC-OCV relationship is not directly observable but can be approximated by taking the average between the charge and discharge curves, resulting in the SOC-OCV curve shown in Figure 4-6.

Along with the charge and discharge curves, the open-circuit voltage also monotonically increases with increasing SOC and can be used as a state-of-charge estimator.

4-3-3 Ordinary least squares

The SOC-OCV relationship can be included in the equivalent circuit model, derived in Section 4-1, by fitting a function to the processed SOC-OCV data. The relationship is highly nonlinear, so linear or affine functions are not sufficient to represent the OCV curve over the entire SOC range [38, 39]. Instead, a polynomial model can be used, formulated as

$$\mathrm{OCV}(z[k]) = \sum_{l=0}^{n_p} p_l z[k]^l \tag{4-20}$$

Where $z[k]$ is the SOC at time step k and n_p is the degree of the polynomial function. p_l are entries of the vector $p \in \mathbb{R}^{n_p \times 1}$ which are the polynomial coefficients. The polynomial function is linear in the coefficients and can be solved using a least squares approach. To solve for p, the polynomial is written in the following format

$$\mathrm{Y} = Hp + \varepsilon \tag{4-21}$$

Where Y is a vector of length N filled with the open-circuit voltage values and N is the number of data points. Hp is the linear model set by the polynomial, with H being a $N \times n_p$ matrix filled with SOC data points in the following format

$$H = \begin{pmatrix} 1 & z[0] & z[0]^2 & \cdots & z[0]^{n_p} \\ 1 & z[1] & z[1]^2 & \cdots & z[1]^{n_p} \\ \vdots & \vdots & \vdots & \ddots & \vdots \\ 1 & z[N] & z[N]^2 & \cdots & z[N]^{n_p} \end{pmatrix} \tag{4-22}$$

Lastly, ε is the error between the assumed model structure and the actual data points. The coefficients p can be found with the least squares method by finding the values $\hat{p}$ that minimize the squared error between the model and the data points, which gives the objective function

$$\min_p J = \min_p \varepsilon^\top \varepsilon = \min_p (\text{OCV} - Hp)^\top (\text{OCV} - Hp) \tag{4-23}$$

The minimum is found by taking the partial derivative with respect to p and setting it equal to zero, yielding

$$\frac{\partial J}{\partial p} = -H^\top (\text{OCV} - H\hat{p}) = 0$$

Expanding the terms and moving the OCV term to the right gives

$$H^\top H\hat{p} = H^\top \text{OCV}$$

The optimal value for p is then found via

$$\hat{p} = \left(H^\top H\right)^{-1} H^\top \text{OCV} \tag{4-24}$$

which is known as the closed-form ordinary least squares (OLS) solution.

4-4 Hysteresis Model

In most Li^+ chemistries, voltage hysteresis is small and can be ignored in identification and state estimation frameworks. Nevertheless, hysteresis models do exist. One of these is the Plett single-state model [10]. In this model, the hysteresis voltage is built up from two components, a dynamic hysteresis, varying with the state-of-charge, and an instantaneous hysteresis.

4-4-1 Instantaneous hysteresis

The instantaneous hysteresis is a simple representation and only depends on the sign of the current and a scaling parameter M_0. When no current is applied, the instantaneous hysteresis does not disappear but equals the previous instantaneous hysteresis. Mathematically, this can be written as

$$V_{h_{inst}}[k] = \begin{cases} M_0 \text{sgn}(i[k]) & |i[k]| > 0 \\ V_{h_{inst}}[k-1] & \text{otherwise} \end{cases} \tag{4-25}$$

Where $V_{h_{inst}}$ is the instantaneous hysteresis voltage and sgn is the sign function, which outputs 1 when the argument is positive and -1 when the argument is negative. The instantaneous hysteresis is thus always either $-M_0$ or M_0.

4-4-2 Dynamic hysteresis

Besides the instantaneous effect, hysteresis is a function of the change in SOC, which can be represented as

$$\frac{\mathrm{d}V_{h_{dyn}}}{\mathrm{d}z} = \bar{\gamma}\mathrm{sgn}(\dot{z})(M(z,\dot{z}) - V_{h_{dyn}}) \tag{4-26}$$

Where $V_{h_{dyn}}$ is the dynamic hysteresis voltage and $\bar{\gamma}$ is the hysteresis rate. $M(z,\dot{z})$ is the maximum dynamic hysteresis as a function of SOC and the time derivative of SOC. The rate of change is proportional to the distance between the current dynamic hysteresis and the maximum dynamic hysteresis [1]. The $\mathrm{sgn}(\dot{z})$ term guarantees stability regardless of the current sign.

The dynamic hysteresis can be rewritten to an ordinary differential equation with respect to time by multiplying both sides with $\mathrm{d}z/\mathrm{d}t$, yielding

$$\dot{V}_{h_{dyn}} = \frac{\mathrm{d}V_{h_{dyn}}}{\mathrm{d}z}\frac{\mathrm{d}z}{\mathrm{d}t} = \bar{\gamma}\mathrm{sgn}(\dot{z})(M(z,\dot{z}) - V_h)\frac{\mathrm{d}z}{\mathrm{d}t}$$

Filling in the continuous-time coulomb equation for $\mathrm{d}z/\mathrm{d}t$ gives

$$\dot{V}_{h_{dyn}} = -\bar{\gamma}\left|\frac{\eta}{3600C}i\right| V_{h_{dyn}} + \bar{\gamma}\left|\frac{\eta}{3600C}i\right| M(z,\dot{z})$$

The parameters η and C are always positive values and are slowly time-varying, so the above relationship can be written in a more compact form by redefining the hysteresis rate to $\gamma = \bar{\gamma}\eta/(3600C)$, which results in

$$\dot{V}_{h_{dyn}} = -\gamma\,|i|\,V_{h_{dyn}} + \gamma\,|i|\,M(z,\dot{z}) \tag{4-27}$$

This differential equation can be discretized in a similar way as the polarization voltage equation, resulting in the difference equation

$$V_{h_{dyn}}[k+1] = e^{-\gamma T_s|i[k]|}V_{h_{dyn}}[k] + \left(e^{-\gamma T_s|i[k]|} - 1\right)M(z,\dot{z}) \tag{4-28}$$

Where T_s is the sampling time, which is now included in the equation. The last step is to define a function $M(z,\dot{z})$ that approximates the behavior of the hysteresis loop. From the behavior of hysteresis in the SOC-OCV curve in Section 4-3, the maximum hysteresis should be positive during charging, since the measured terminal voltage is generally higher than the OCV during charge, and negative during discharging, where the opposite is true. A simple maximum hysteresis function can then be realized as

$$M(z,\dot{z}) = -M\mathrm{sgn}(i[k])$$

Where M is the maximum hysteresis value. Since the current is defined as positive during discharging this equation complies with the expected sign of the dynamic hysteresis. Filling in this formula into the dynamical equation gives

$$V_{h_{dyn}}[k+1] = e^{-\gamma T_s|i_k|}V_{h_{dyn}}[k] + M\left(e^{-\gamma T_s|i_k|} - 1\right)\mathrm{sgn}\left(i[k]\right) \tag{4-29}$$

Which is the final form of the discrete-time dynamic hysteresis. The total hysteresis as described by the Plett single-state model can then be found by summing the dynamic and instantaneous hysteresis voltages,

$$V_h[k] = V_{h_{inst}} + V_{h_{dyn}} \tag{4-30}$$

The total hysteresis voltage is included in the terminal voltage equation by adding it to the right-hand side, which gives

$$V_t[k] = \text{OCV}[k] + V_h[k] - V_p[k] - R_0 i[k] \tag{4-31}$$

Where the hysteresis is positive during charging and negative when discharging, corresponding with the voltage observations in Figure 4-6.

Chapter 5

Identification & State Estimation

Estimating and then tracking the states and parameters of a lithium-ion battery cell requires the use of state estimation frameworks. In pursuit of this goal, this work applies an adaptive method, the joint unscented Kalman filter, in combination with previously derived mathematical models of the Li^+ cell from Chapter 4.

First, the unscented Kalman filter algorithm is introduced and its three main steps are broken down and explained. Afterward, a method is described to combine the mathematical models of a lithium-ion cell with an unscented Kalman filter to perform identification and state estimation in real time.

In total, three variations on the basic RC equivalent circuit are defined:

- One RC-pair model with a predetermined SOC-OCV relationship (RC).
- One RC-pair model with a predetermined SOC-OCV relationship and voltage hysteresis (RC-H).
- One RC-pair model with an adaptive SOC-OCV relationship and voltage hysteresis (A-RC-H).

The models will be referred to by their abbreviations, RC, RC-H, and A-RC-H (can be pronounced as 'arch').

5-1 Unscented Kalman Filter

The unscented Kalman filter (UKF) is part of the sigma point Kalman filter (SPKF) family and is capable of handling nonlinear systems, similarly to the extended Kalman filter (EKF). The main advantage of the UKF over the EKF is that it can represent Gaussian nonlinearities with at least third-order accuracy, while the Taylor approximations in the EKF are only first-order accurate. When inputs are non-Gaussian, at least a second-order accuracy is guaranteed [40].

5-1-1 Sigma points

The UKF achieves third-order accuracy by using the unscented transform (UT) to take samples around the predicted states, called sigma points. The UT can approximate the actual mean and covariance of the system with higher fidelity compared to the EKF. The UT process is shown and compared with the EKF in Figure 5-1, from [40].

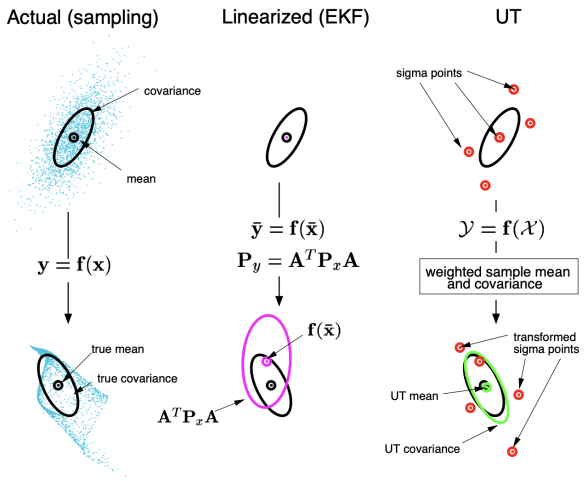

Figure 5-1: Mean and covariance propagation using UT, compared with actual distribution and the EKF approximation [40].

5-1-2 Overview

The UKF is initialized by guessing an initial set of states and a state covariance matrix that represents the uncertainty in the correctness of the initial states. To fit the two-phase structure of the UKF, the initial conditions are defined as the corrected states at time index -1, which are $x^+[k-1]$, and the corrected state uncertainty $P^+[k-1]$. Model predictions are denoted by $^-$. While the superscript $^+$ denotes estimations that have been corrected by the filter.

The last initialization step is to specify a process noise covariance matrix Q and a measurement noise covariance matrix R. Both are typically chosen to be square, diagonal, and positive definite matrices, representing Gaussian noise in the process/model and the measurements, which are assumed to be uncorrelated with each other. Their dimensions are determined by the number of states and the number of outputs in the system, i.e. $Q \in \mathbb{R}^{n_x \times n_x}$ and $R \in \mathbb{R}^{n_y \times n_y}$.

After initialization, the UKF can be divided into two phases that are executed at each time index k:

1. Prediction - The sigma points $\mathcal{X}[k-1]$ are generated with the corrected states and the corrected state uncertainty from the previous time index, $x^+[k-1]$ and $P^+[k-1]$. Each of the sigma points is propagated separately using the state equation and sigma point outputs are computed by inserting the propagated sigma points into the measurement

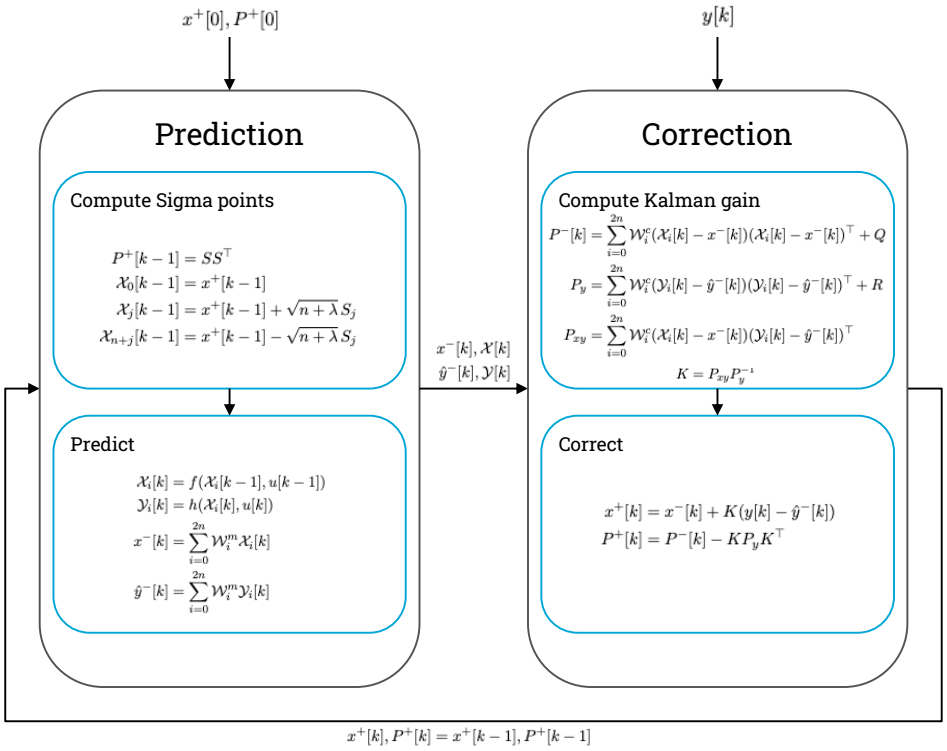

Figure 5-2: Flowchart of the unscented Kalman filter algorithm.

equation. The propagated sigma points and outputs are then weighted to compute the predicted states $x^-[k]$ and the predicted outputs $\hat{y}^-[k]$.

2. Correction - The predictions are used to compute covariance matrices, which then determine the Kalman gain, a weighing matrix that balances model predictions and measurements. Using the Kalman gain, the predicted states, the predicted outputs, and the measurements are combined into the corrected states $x^+[k]$ and the corrected state uncertainty matrix P^+.

The algorithm repeats during every time step, using the previous corrected states and uncertainty to initialize the next prediction step. A flowchart of the algorithm is shown in Figure 5-2. The following subsections provide more details for each phase of the UKF.

5-1-3 Prediction

Sigma points are generated with the square root of the corrected state uncertainty matrix P^+, but taking the square root of a matrix directly is not well-defined and can lead to numerical instability. The alternative is to use the Cholesky decomposition of P^+, which defines a lower triangular matrix S such that

$$P^+[k-1] = SS^\top \tag{5-1}$$

In this work, S was determined using the `chol` function in MATLAB. The sigma points are then sampled around the corrected states $x^+[k-1]$ using S, resulting in $2n+1$ sets of sigma points described by

$$\mathcal{X}_0[k-1] = x^+[k-1] \tag{5-2}$$
$$\mathcal{X}_j[k-1] = x^+[k-1] + \sqrt{n+\lambda}\, S_j \tag{5-3}$$
$$\mathcal{X}_{n+j}[k-1] = x^+[k-1] - \sqrt{n+\lambda}\, S_j \tag{5-4}$$
$$j \in [1, n] \tag{5-5}$$

Here, $S_j^\top$ denotes the j-th column of $S^\top$ and n is the number of states in the model. λ is a constant and is initialized as

$$\lambda = n(\alpha^2 - 1) \tag{5-6}$$

Where α is a hyperparameter that determines the spread of the sigma point sampling around the state estimate, which is typically confined to $1e-4 \leq \alpha \leq 1$ [41]. For all UKF implementations in this work, α was set to $1e-3$. Each sigma point is propagated one step ahead via

$$\mathcal{X}_i[k] = f(\mathcal{X}_i[k-1], u[k-1]) \tag{5-7}$$
$$i \in [0, 2n] \tag{5-8}$$

Where $f(\cdot)$ is the state transition function of the dynamical system. These propagated points are recombined into a prediction of the state $x^-[k]$ via

$$x^-[k] = \sum_{i=0}^{2n} \mathcal{W}_i^m \mathcal{X}_i[k] \tag{5-9}$$

$\mathcal{W}_i^m$ are entries of the mean weighting vector $\mathcal{W}^m$. The weights can be determined in multiple ways [40, 42]. In this work, the weights are defined as [40]

$$\mathcal{W}^m = \begin{pmatrix} \frac{\lambda}{n+\lambda} & \frac{1}{2(n+\lambda)} & \cdots & \frac{1}{2(n+\lambda)} \end{pmatrix} \in \mathbb{R}^{1\times 2n+1} \tag{5-10}$$

The predicted output is found in a similar way. First, the output sigma points $\mathcal{Y}$ are found by inserting each sigma point into the measurement equation $h(\cdot)$ as

$$\mathcal{Y}_i[k] = h(\mathcal{X}_i[k], u[k]) \tag{5-11}$$
$$i \in [0, 2n] \tag{5-12}$$

The predicted output $\hat{y}^-$ is then computed by weighing the output sigma points

$$\hat{y}^-[k] = \sum_{i=0}^{2n} \mathcal{W}_i^m \mathcal{Y}_i[k] \tag{5-13}$$

5-1-4 Correction

The next step is to correct the prediction by combining it with a measurement $y[k]$ and known statistics. First, the state prediction uncertainty matrix $P^-[k]$ is computed as

$$P^-[k] = \sum_{i=0}^{2n} \mathcal{W}_i^c (\mathcal{X}_i[k] - x^-[k])(\mathcal{X}_i[k] - x^-[k])^\top + Q \tag{5-14}$$

Which uses the predicted states, the propagated sigma points, and the process noise covariance matrix Q. $\mathcal{W}_i^c$ are entries of the covariance weighting vector, which is defined as [41]

$$\mathcal{W}^c = \begin{pmatrix} \frac{\lambda}{n+\lambda} + (1 - \alpha^2 + \beta) & \frac{1}{2(n+\lambda)} & \cdots & \frac{1}{2(n+\lambda)} \end{pmatrix} \in \mathbb{R}^{1 \times 2n+1} \tag{5-15}$$

Where β is another constant. When assuming a Gaussian distribution, $\beta = 2$ is the optimal choice [40]. The output prediction uncertainty P_y is computed in a similar way, namely

$$P_y = \sum_{i=0}^{2n} \mathcal{W}_i^c (\mathcal{Y}_i[k] - \hat{y}^-[k])(\mathcal{Y}_i[k] - \hat{y}^-[k])^\top + R \tag{5-16}$$

Which is determined using the predicted outputs, the output sigma points, and the measurement noise covariance matrix R. The last covariance matrix to compute is the cross-covariance matrix between the states and the outputs

$$P_{xy} = \sum_{i=0}^{2n} \mathcal{W}_i^c (\mathcal{X}_i[k] - x^-[k])(\mathcal{Y}_i[k] - \hat{y}^-[k])^\top \tag{5-17}$$

The Kalman gain K is then described by

$$K = P_{xy} P_y^{-1} \tag{5-18}$$

The prediction correction is based on the Kalman gain and the current output error, defined as

$$x^+[k] = x^-[k] + K(y[k] - \hat{y}^-[k]) \tag{5-19}$$

The Kalman gain is effectively a weighing matrix that dynamically determines a balance between trusting the measurements and trusting the model predictions. The final part of the correction step is to prepare for the next UKF iteration by updating the state correction uncertainty P^+ via

$$P^+[k] = P^-[k] - K P_y K^\top \tag{5-20}$$

The covariance matrix P only has a unique Cholesky decomposition when it is symmetric and positive definite. Numerical errors in the iterative computation of P^+ can affect these properties, causing the MATLAB `chol` function to fail. One solution to this problem is to use an extension to the original UKF, the square-root UKF (SR-UKF). The SR-UKF propagates the square-root covariance matrix S forward in time, instead of P, which leads to better numerical robustness [41]. A simpler solution that should also lead to better robustness is to preserve symmetry by using the transpose of P^+ and adjusting P^+ after the correction step in Equation 5-20 with

$$P^+[k] = \frac{1}{2} P^+[k] + \frac{1}{2} P^+[k]^\top \tag{5-21}$$

5-2 Identification & State Estimation Framework

The unscented Kalman filter can be applied to the battery cell identification and state estimation problem by combining the general algorithm with a mathematical model of the cell that contains all relevant states and parameters. The RC equivalent circuit model derived in Section 4-1 is capable of linking current and terminal voltage measurements to the circuit parameters, but fails to describe the state-of-charge dynamics, which is a key state that should be estimated. To remedy this, the coulomb counting equation, Equation 4-14, is added to the RC model structure. This links the identification of circuit parameters to the estimation of the SOC but also allows any error sources in the coulomb counting equation to be implicitly corrected by the long-term stable SOC-OCV relationship.

The regular UKF formulation, as described in Section 5-1, requires model states to have dynamical equations that can be summarized in a state transition function $x[k] = f(x[k-1], u[k-1])$ and a measurement function $y[k] = h(x[k], u[k])$. The coulomb counting equation and polarization voltage formula have this format, but the time-varying parameters do not have easily defined dynamical equations. Luckily, the UKF can be modified to include the estimation of time-varying parameters by using heavily simplified dynamical models. By defining the original states as the vector ξ and the parameters as the vector θ, the vectors can be appended together to form a new joint state vector x, given by

$$x = \begin{pmatrix} \xi \\ \theta \end{pmatrix}$$

The time evolution of the parameters is described via

$$\theta[k] = \theta[k-1] + w_\theta[k]$$

Where $w_\theta[k]$ is the process noise in the parameters, assumed to be Gaussian. This model structure assumes that the current parameter value is close to the previous value. This combination of states and parameters in a UKF is sometimes referred to as the joint unscented Kalman filter (JUKF). Although the parameter dynamics are extremely simple, it allows for the state estimation and parameter identification to be performed simultaneously without changing the UKF framework.

The next step is to define a state transition function $f(x, u)$ and a measurement function $h(x, u)$, which are both needed in the filter. Depending on which model is used ξ, θ, $f(x, u)$, and $h(x, u)$ will vary. In all equations, the input u is taken to be the current going through the battery i, and the measurement y is equal to the terminal voltage V_t.

5-2-1 RC model

The simplest model using the RC equivalent circuit is a one-pair RC model. As derived in Section 4-1, this model has three circuit parameters, the ohmic resistance, the RC time constant, and the polarization resistance. θ can then be defined as

$$\theta = \begin{pmatrix} R_0 & \tau & R_p \end{pmatrix}^\top$$

In order to estimate state-of-charge, the coulomb counting equation, described in Section 4-2 is included in the model, leading to two states in total, the state-of-charge and the polarization voltage. This defines ξ as

$$\xi = \begin{pmatrix} z & V_p \end{pmatrix}^\top$$

The complete joint state vector then becomes

$$x = \begin{pmatrix} z & V_p & R_0 & \tau & R_p \end{pmatrix}^\top$$

The state transition function combines the dynamical relationship of the SOC and the polarization voltage, as derived in Chapter 4, with the simple propagation of the parameters into a vector, which gives the function

$$x[k] = f(x[k-1], u[k-1]) = \begin{pmatrix} z[k-1] - T_s \frac{1}{3600C} u[k-1] \\ e^{-T_s/\tau[k-1]} V_p[k-1] + R_p[k-1] \left(1 - e^{-T_s/\tau[k-1]}\right) u[k-1] \\ R_0[k-1] \\ \tau[k-1] \\ R_p[k-1] \end{pmatrix} \tag{5-22}$$

Note that the coulombic efficiency η is neglected here in the coulomb counting equation. This is a valid approximation on short timescales because the coulombic efficiency of Li^+ cells is generally high [1]. Lastly, the measurement function of the RC model is formulated as

$$y[k] = h(x[k], u[k]) = \text{OCV}(z[k]) - V_p[k] - R_0 u[k] \tag{5-23}$$

Where $\text{OCV}(\cdot)$ is the nonlinear SOC-OCV function discussed in Section 4-3.

5-2-2 RC-Hysteresis model

The RC-Hysteresis (RC-H) model is an extension of the RC model and attempts to model voltage hysteresis by including a model for the dynamic soc-varying hysteresis. This model neglects the instantaneous hysteresis, as its inclusion was deemed to be negligible to model performance after initial testing, meaning the voltage hysteresis is given by

$$V_h[k] = V_{h_{inst}} + V_{h_{dyn}} \approx V_{h_{inst}}$$

The dynamic hysteresis voltage is modeled using the difference equation derived in Section 4-4, which adds two parameters, the hysteresis rate γ and the maximum hysteresis M, to the parameter vector, turning θ into

$$\theta = \begin{pmatrix} R_0 & \tau & R_p & \gamma & M \end{pmatrix}^\top$$

With the addition of the hysteresis voltage V_h, the state vector becomes

$$\xi = \begin{pmatrix} z & V_p & V_h \end{pmatrix}^\top$$

The joint state vector for the RC-Hysteresis vector then becomes

$$x = \begin{pmatrix} z & V_p & V_h & R_0 & \tau & R_p & \gamma & M \end{pmatrix}^\top$$

The state transition function is similar to the RC model, but now includes the difference equation for the dynamic hysteresis voltage, which turns $f(x,u)$ into

$$f(x[k-1],u[k-1]) = \begin{pmatrix} z[k-1] - T_s \frac{1}{3600C} u[k-1] \\ e^{-T_s/\tau[k-1]} V_p[k-1] + R_p[k-1]\left(1 - e^{-T_s/\tau[k-1]}\right) u[k-1] \\ e^{-\gamma[k-1]T_s|u[k-1]|} V_h[k-1] + M[k-1]\left(e^{-\gamma[k-1]T_s|u[k-1]|} - 1\right) \operatorname{sgn}(u[k-1]) \\ R_0[k-1] \\ \tau[k-1] \\ R_p[k-1] \\ \gamma[k-1] \\ M[k-1] \end{pmatrix} \tag{5-24}$$

The measurement function is modified by adding the voltage hysteresis state, which has a positive effect on the terminal voltage. $h(x,u)$ then becomes

$$h(x[k],u[k]) = \text{OCV}(z[k]) + V_h[k] - V_p[k] - R_0 u[k] \tag{5-25}$$

5-2-3 Adaptive-RC-Hysteresis model

As discussed in Section 4-3, estimating the SOC-OCV relationship requires time-consuming laboratory tests with expensive equipment. The relationship is also dependent on temperature and drifts over time as the battery cell ages. It might then be beneficial to forego the OCV tests and instead estimate the SOC-OCV relationship online using the RC equivalent circuit model and the joint unscented Kalman filter.

One method is to include the polynomial coefficients from a high-order polynomial function into the joint state vector and estimate the entire polynomial function using the JUKF. However, in practice, this does not lead to good results for the state and parameter estimations. The joint UKF has difficulty converging with so many parameters and the high-order polynomial function fit is meant for a global representation of the OCV over the entire SOC range. The JUKF corrects the states and parameters in real-time and is "blind" to this global optimality. Instead, the SOC-OCV is locally approximated by an affine function of the form

$$\text{OCV}(z[k]) = c_0 + c_1 z[k] \tag{5-26}$$

This represents a local linearization of the SOC-OCV curve, where only two coefficients, c_0 and c_1, need to be estimated by the JUKF. This local SOC-OCV function reconstruction can be combined with the previously derived RC-H model by simply replacing the $\text{OCV}(z[k])$ function with Equation 5-26. This is referred to as the adaptive-RC-Hysteresis (A-RC-H)

model. The A-RC-H functions can be written as

$$f(x[k-1],u[k-1]) = \begin{pmatrix} z[k-1] - T_s \frac{1}{3600C} u[k-1] \\ e^{-T_s/\tau[k-1]} V_p[k-1] + R_p[k-1]\left(1 - e^{-T_s/\tau[k-1]}\right) u[k-1] \\ e^{-\gamma[k-1]T_s|u[k-1]|} V_h[k-1] + M[k-1]\left(e^{-\gamma[k-1]T_s|u[k-1]|} - 1\right) \operatorname{sgn}(u[k-1]) \\ R_0[k-1] \\ \tau[k-1] \\ R_p[k-1] \\ \gamma[k-1] \\ M[k-1] \\ c_0[k-1] \\ c_1[k-1] \end{pmatrix} \tag{5-27}$$

$$h(x[k],u[k]) = c_0[k] + c_1[k]z[k] + V_h[k] - V_p[k] - R_0 u[k] \tag{5-28}$$

Which has the joint state vector

$$x = \begin{pmatrix} z & V_p & V_h & R_0 & \tau & R_p & \gamma & M & c_0 & c_1 \end{pmatrix}^\top$$

5-2-4 SOC initialization

The Kalman filter requires a guess of the initial state-of-charge to kick-start the algorithm, which can greatly affect the accuracy of the SOC estimation but is generally unknown. When starting the filter during a no-load resting phase, however, the voltage measurements are close to the actual OCV and can be used to guess the SOC, assuming that the remaining polarization and voltage hysteresis only contribute a small amount to the terminal voltage.

This can be achieved with an inverse function of the SOC-OCV relationship, $z = \mathrm{OCV}'(V_t)$ or by using a root-finding algorithm like the Newton-Rhapson method, which is an iterative method that tries to find a value z that solves the equation $\mathrm{OCV}(z) - V_t = 0$. At iteration i, the method finds the next z_{i+1} according to

$$z_{i+1} = z_i - \frac{\mathrm{OCV}(z_i) - V_t}{\mathrm{OCV}'(z_i)} \tag{5-29}$$

Where $\mathrm{OCV}'(z)$ is the derivative of $\mathrm{OCV}(z)$. Assuming the OCV function is a polynomial, the derivative is trivial to derive. The Newton-Rhapson method again requires an initial value for z, but a reasonable guess of 50% SOC, the middle of the SOC range, is enough for the algorithm to converge to correct values around 100% SOC within 5-10 iterations. A downside of the Newton-Rhapson algorithm is the possibility of a singularity in the fraction when the derivative equals zero or a large change in the estimation when the derivative is very small.

The assumption that polarization and hysteresis are small enough such that the SOC initialization is reasonably accurate, might not always be the case. Therefore, Section 6-4 investigates the effect of significant initial SOC errors on the performance of the SOC estimation.

Chapter 6

Results

This chapter details the results of applying the three different models to a lithium-ion battery data set produced by the EVERLASTING project, which subjected several lithium-ion battery cells to aging tests over an almost one-year period [14]. The cells have a nominal capacity of 3.5 Ah and have an NMC positive electrode with a negative electrode made from silicon-doped graphite (NMC/Si-C). In between aging cycles, extensive check-up tests are performed that include C/20 and dynamic stress tests. The C/20 tests are used to estimate the total capacity and the SOC-OCV relationship. To limit the scope of this work, data from only one cell was used, cell 88.

First, the SOC-OCV relationship is established and aging effects are discussed. Then the dynamic profiles are introduced that will be used to identify battery states and parameters. After a discussion on the tuning strategy, the three models are tested and JUKF residuals, SOC estimations, and ohmic resistance estimations are discussed. Section 6-7 summarizes the model performance by comparing the SOC estimation accuracies using several performance metrics. Finally, the three models are tested on the same cell but after significant aging. The Kalman filter is tuned based on the begin-of-life dynamic profiles, so the aged data acts as a validation of the framework and the filter tuning.

6-1 SOC-OCV Relationship

This section shows the process of identifying the SOC-OCV relationship using C/20 tests performed at an ambient temperature of 25°C. First, the data is analyzed and processed to create voltage curves as a function of SOC. The final polynomial degree for the SOC-OCV function is chosen by evaluating several polynomial functions with varying degrees, fitted on the BOL SOC-OCV data. The chapter concludes with an investigation of the fade in total capacity and SOC-OCV drift as the battery cell ages.

6-1-1 Data analysis

The original data set uses a variable sampling time, mostly with a sampling time of 60 seconds, but with a sampling time of less than a second in other places. For consistency, the data was transformed to an equally-spaced grid with a sampling time of 1 s using interpolation with MATLAB's `interp1` function. The impact of processing the data on the accuracy of the capacity estimation and SOC-OCV relationship determination was tested and determined to be negligible.

The C/20 tests start from a fully charged cell and then discharge until 0% SOC. The cell is then rested for 1 hour before charging the cell back to 100% again. The resulting voltage and current data are shown in Figure 6-1. The total experiment time is about 40 hours. The cell has a maximum voltage of 4.2 V and was charged to 100% using a full CC-CV profile and then rested. At the start of the C/20 test, however, the cell voltage is about 4.185 V. This has to do with the voltage decreasing slightly due to depolarization, no ohmic loss, and thermal relaxation. The plot shows the voltage decreasing as the SOC decreases, with a large rate of decrease at low SOC. The current is cut when the minimum voltage is reached at 2.5 V, where the SOC is defined to be zero. During the resting period, the terminal voltage increases again due to the absence of ohmic losses, depolarization, and thermal relaxation. The cell is then charged until 4.2 V, where the cell is at 100% SOC again.

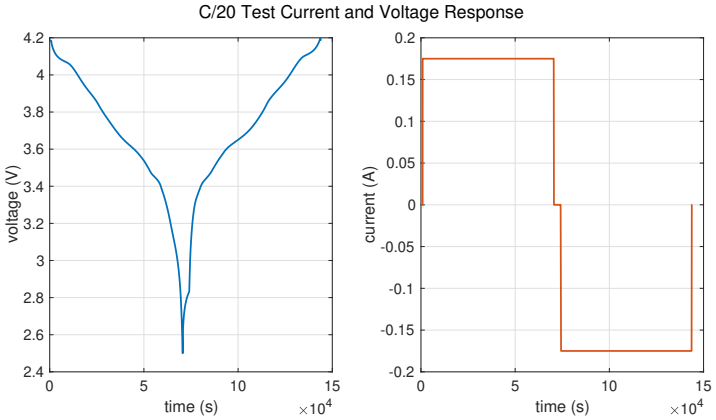

Figure 6-1: Voltage and current data during a C/20 test.

The amount of charge going in and going out is computed by summing the charge and discharge currents, multiplying by the sampling time (set to 1 s), and dividing by 3600 to convert the units to Ah. For discharge, the charge going out is defined as the total capacity and equaled 3.387 Ah. The total charge going in was found to be 3.382 Ah, which results in a coulombic efficiency of 1.0015. The coulombic efficiency should always be less than or equal to one, but due to the high efficiency of Li^+ cells and experimental error, the efficiency can sometimes be slightly larger than one [1]. This coulombic efficiency is still used in the remainder of the process. With the coulombic efficiency and the total capacity, the voltage curves can be processed and plotted as a function of SOC, which is shown in Figure 6-2.

Under the assumption that voltage losses and hysteresis are small and approximately equal for both charge and discharge, the average curves can be used to approximate the open-circuit voltage of the cell. To average the curves, they have to be interpolated on an equally-spaced

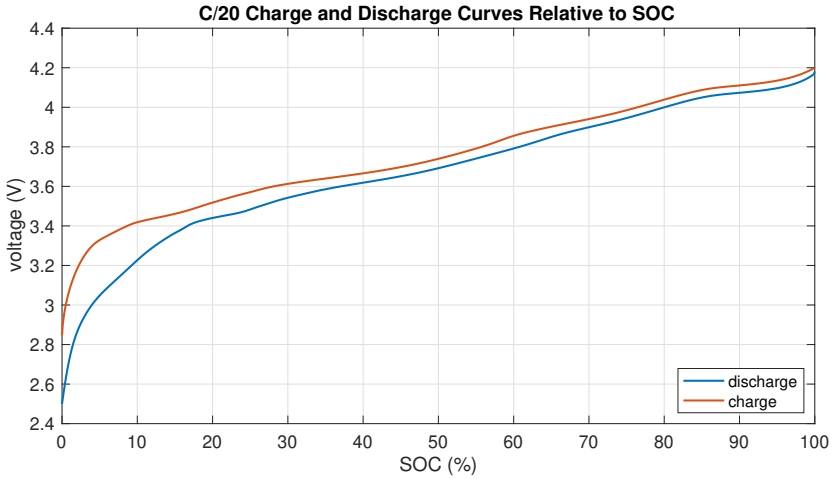

Figure 6-2: C/20 charge and discharge curve relative to SOC.

grid first, such that their data points have the same SOC values. Then the OCV points are found by summing the voltages at each data point and dividing them by two. The resulting OCV plot is shown in Figure 6-3.

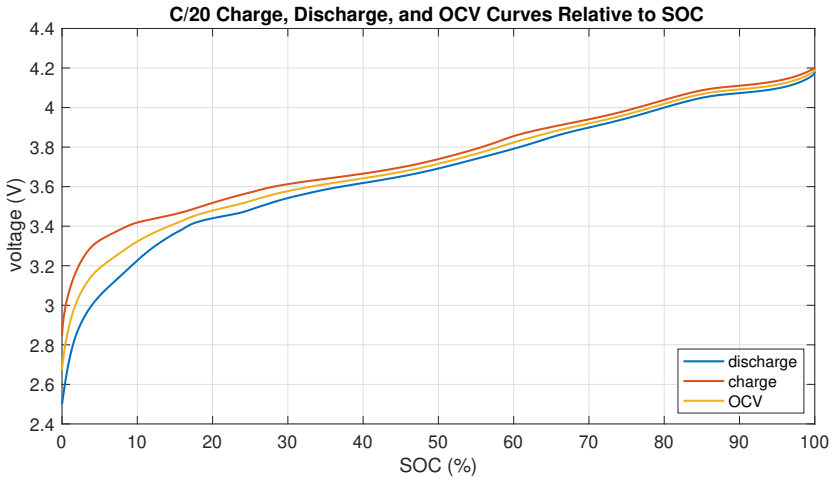

Figure 6-3: C/20 charge, discharge, and OCV curve relative to SOC.

6-1-2 Function fitting

The OCV curve is fitted using the ordinary least squares solution of a polynomial function. The degree of the polynomial n_p is chosen by comparing several different fits. Figure 6-4 shows the comparison with six different polynomial functions and Table 6-1 shows their root-mean-square error (RMSE). The RMSE is a common performance metric and is computed as

$$\text{RMSE} = \sqrt{\frac{1}{N}\sum_{i=0}^{N} e_i^2} \tag{6-1}$$

Table 6-1: Comparison of RMSE values for different polynomial degrees.

Degree	5	6	7	8	9	10
RMSE (mV)	17.59	16.37	13.08	11.27	7.123	6.851

Where N is the number of data points and e is the error between each data point and the corresponding estimated value. Low RMSE values are indicative of high performance. All fits capture the SOC-OCV relationship with good performance and their root-mean-square error (RMSE) decreases with increasing n_p due to the larger degrees of freedom.

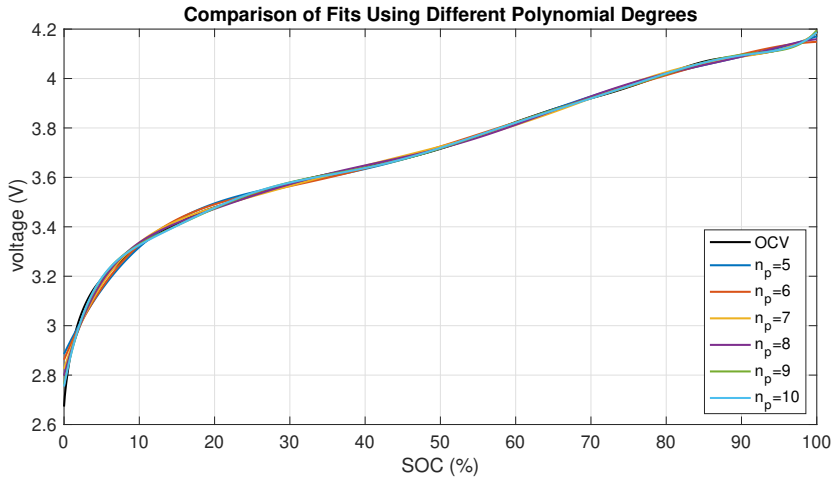

Figure 6-4: Comparison of fits using different polynomial degrees.

However, minimizing the RMSE should not be the only objective. When plotting the error, in Figure 6-5, it can be seen that the performance of all models degrades heavily as the SOC approaches zero, and some models have difficulty portraying the curve at high SOC. In normal battery operation, low SOC, < 0.1, is typically never reached because the cut-off voltage is hit much earlier due to ohmic losses. This means that bad performance at low SOC is usually acceptable. However, high SOC is reached during normal operation and good performance of the polynomial in that region is desired.

By magnifying the high SOC range in Figure 6-5, Figure 6-6 can be plotted, which shows that 7 and 10 best describe the high SOC behavior. Interestingly, 8 and 9 have a lower RMSE value than 7, but perform worse than 7 at high SOC.

In real-time battery management systems, the SOC-OCV function implementation is often constrained by computational memory resources, which turns the choice of polynomial degree into a trade-off between memory size and performance. In this work, computational and memory efficiency was not a primary goal, and accuracy is preferred over computational complexity, so a polynomial degree of 10 is chosen to represent the SOC-OCV relationship. Higher-order polynomials were not considered. The final BOL OCV function can then be

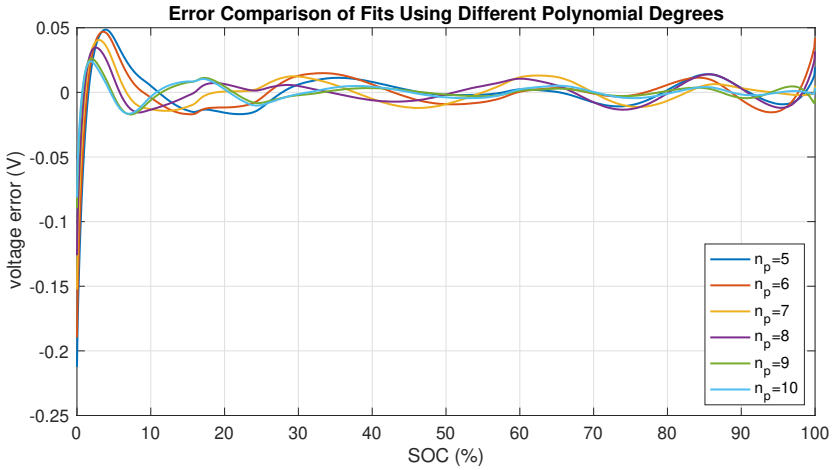

Figure 6-5: Error comparison of fits using different polynomial degrees.

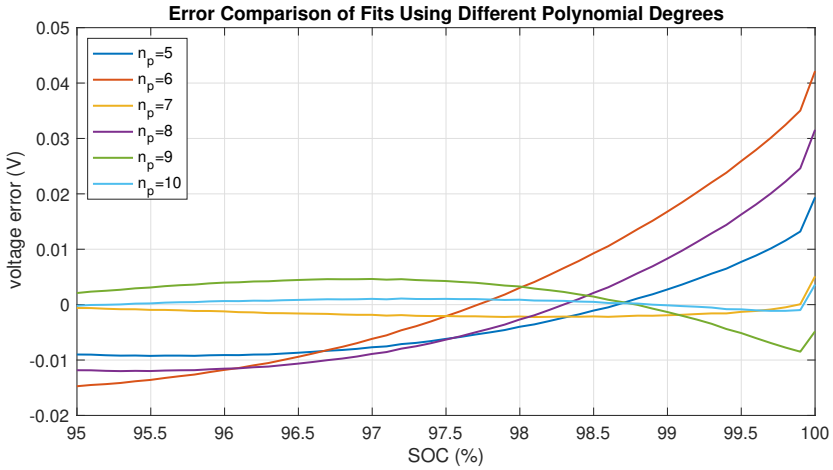

Figure 6-6: Error comparison of fits using different polynomial degrees at high SOC.

written as

$$\begin{aligned}\mathrm{OCV}(z[k]) = 2.754 + 15.63z[k] - 196.8z[k]^2 + 1.492\mathrm{e}3z[k]^3 - 6.734\mathrm{e}3z[k]^4 + 1.884\mathrm{e}4z[k]^5 \\ -3.344\mathrm{e}4z[k]^6 + 3.765\mathrm{e}4z[k]^7 - 2.598\mathrm{e}4z[k]^8 + 9.986\mathrm{e}3z[k]^9 - 1.630\mathrm{e}3z[k]^{10}\end{aligned} \tag{6-2}$$

6-1-3 Aging effects

The SOC-OCV curve drifts as the battery cell ages. The significance of the drift can be investigated by repeating the SOC-OCV identification process for subsequent C/20 tests in the cell 88 data set. First, fade in the total capacity can be visualized by computing the total capacity at every C/20 test, which is shown in Figure 6-7. Following the definition that the first total capacity has 100% capacity state-of-health (SOH_C), the plots show that every aging test reduces the SOH_C by roughly 10%.

Figure 6-8 and Figure 6-9 display the discharge and charge voltage versus SOC curves with

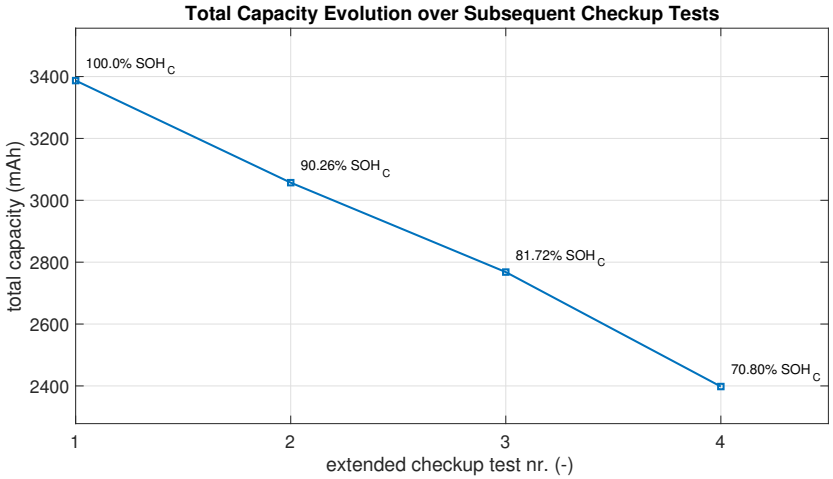

Figure 6-7: Total capacity evolution over subsequent checkup tests.

decreasing SOH_C. Both curves can be seen to drift upward at mid-low SOC as the cell ages. The drift effect is notably smaller in the high SOC region.

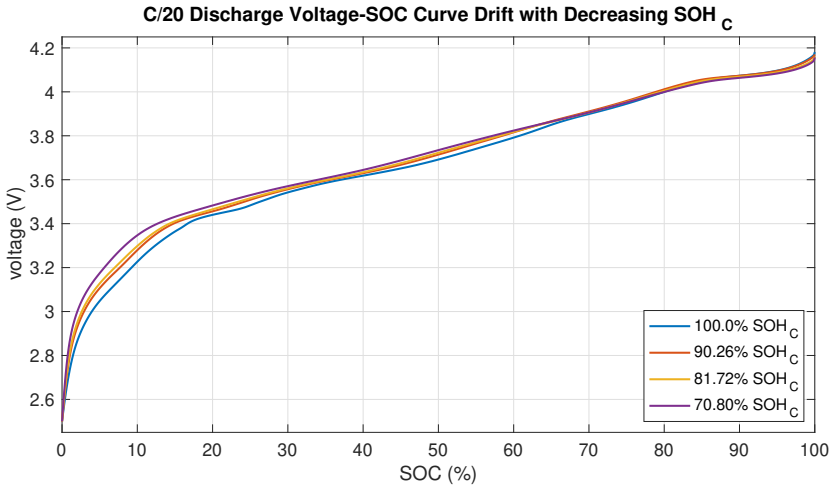

Figure 6-8: C/20 discharge voltage-SOC curve drift with decreasing SOH_C.

Next, the fitted SOC-OCV function is plotted for each C/20 test in Figure 6-10. A clear pattern can be observed. At high SOC the drift is negligible, except near 100% SOC where the voltage decreases slightly with decreasing state-of-health. In the middle and lower SOC range, the effect is much more noticeable and the curves drift upward with decreasing SOH_C. Interestingly, the drift between 90% to 80% SOH_C is much smaller than between 100% to 90% and 80% to 70%, indicating that the effect is not linearly proportional to SOH_C.

When the 100% SOH_C SOC-OCV curve is the sole state-of-charge estimator, the drifting effect can have a large impact on the SOC estimation due to the relative flatness of the curve. In Figure 6-10, this is most apparent at 3.7 V between the 100% and the 70% SOH_C curves. At about this voltage, the 100% curve has an SOC of 50%, while the 70% has roughly an SOC of 40%. The SOC would then be overestimated by about 10% from just SOC-OCV drift.

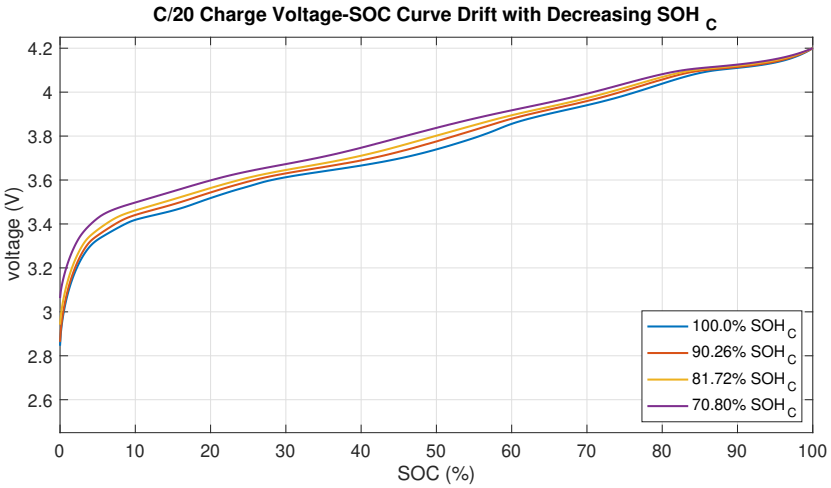

Figure 6-9: C/20 charge voltage-SOC curve drift with decreasing SOH_C.

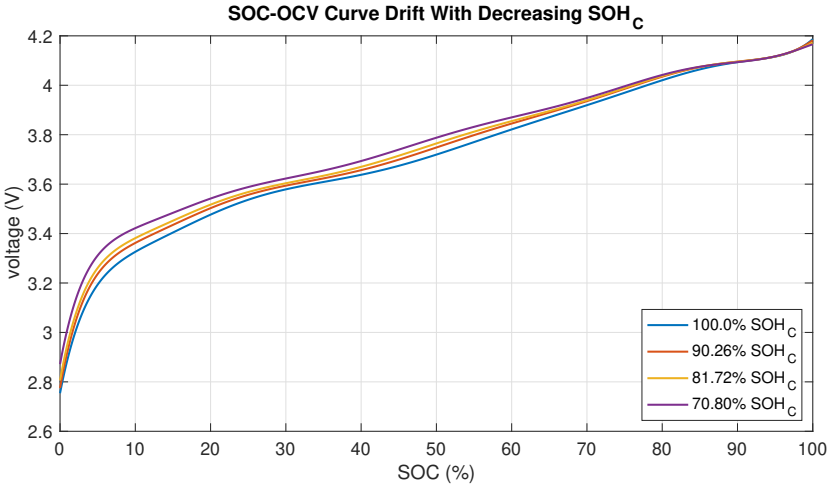

Figure 6-10: SOC-OCV curve drift with decreasing SOH_C.

6-2 Dynamic Profiles

The EVERLASTING project data set uses two different dynamic profiles to test and cycle the battery cell, the dynamic stress test (DST) and a driving cycle test (DCT) [14]. Both tests discharge the cell from 100% SOC to about 10% and are performed at a 25°C ambient temperature. The DST, shown in Figure 6-11, is a common cell test where the current is varied in fixed periods of time, according to a set profile with repeating features. The current pattern is similar in all DSTs but the current magnitude is scaled to the operating limits of the considered cell. Negative/charging currents are also included in the DST.

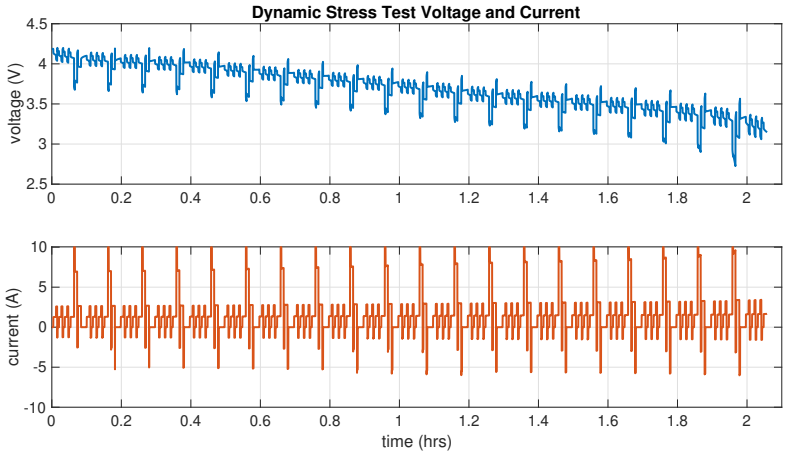

Figure 6-11: Voltage and current data during a dynamic stress test.

The second dynamic profile, the driving cycle test, is graphed in Figure 6-12. The DCT is meant to represent realistic load profiles experienced by electric vehicles and was adapted from data collected from a VOLTIA EV [14]. In comparison to the DST, the current load in the driving cycle is more varied and the current often turns negative for short periods of time. This is representative of the regenerative charging ability of EVs, where some energy is recovered from the electric motors during coasting.

These DST and DCT experiments are performed a relatively short time after the first C/20 test. Therefore it can be assumed that the total capacity during the dynamic tests is equal to the first C/20 test, 3.387 Ah.

Before applying the joint UKF framework to the data, the profiles were transformed to an equally-spaced grid with 1 s time intervals by using MATLAB's `interp1` function.

The baseline for the state-of-charge estimation is computed using the coulomb counting method with an initial SOC of 100%. This baseline is not an exact truth, as the current measurements are never completely accurate and the initial SOC assumption could have a small error. Still, the baseline gives the most accurate representation of the actual SOC and is used to benchmark all SOC estimation results. The SOC error is then computed as the baseline minus the estimate. A positive error thus means an underestimation of the SOC, and a negative error is an overestimation.

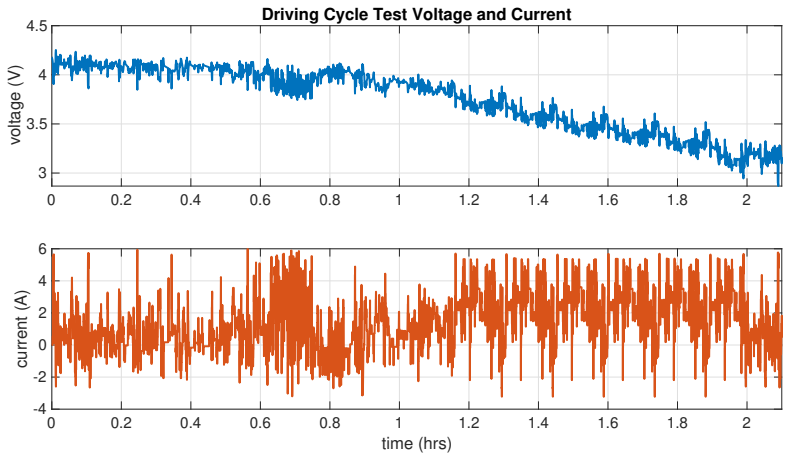

Figure 6-12: Voltage and current data during a driving cycle test.

6-3 Filter Tuning Strategy

Initializing the joint unscented Kalman filter requires an initial state estimate $x^+[0]$, an initial state uncertainty covariance matrix $P^+[0]$, a process noise covariance matrix Q, and a measurement noise covariance R. These can be considered hyperparameters of the JUKF, which have a large impact on the performance of the algorithm, as incorrect tuning can lead to large errors in SOC estimation accuracy. Hyperparameter tuning is therefore done iteratively, based on the first dynamic stress test and driving cycle test.

$x^+[0]$ can be tuned using typical battery cell parameter values. Cell resistances, for example, are often in the range of 0-100 mΩ. The initial uncertainty covariance is assumed to be a diagonal matrix and its entries can be found using the 3-σ principle. Assuming that the probability is normally distributed, the actual value is very likely to be within three standard deviations of the initial guess $x^+[0]$. By setting this 3σ equal to the $\pm$ range where the optimal value is likely to be found, the variance for that state can be found via $(3\sigma/3)^2$. The 3-σ strategy is not guaranteed to be an optimal tuning strategy at all, but it allows for a more systematic way of tuning the uncertainty covariance. The noise covariances, Q and R, were tuned iteratively using factors of 10. Parameter covariances were kept equal for all models wherever possible and R was set to 1e-4 for the RC and RC-H models.

One method to evaluate the tuning is to look at the residual of the JUKF. The residual is computed at every time step by comparing the measurement with the estimated output using the corrected states $x^+[k]$,

$$r[k] = y[k] - h(x^+[k], u[k]) \tag{6-3}$$

In an ideal scenario, the residual should have zero mean. Most of the JUKF tuning was performed using the SOC estimation accuracy during the first dynamic stress test with an initial SOC guess of 90%. Afterward, the tuning was adjusted slightly based on the driving cycle test SOC estimation.

Afterward, the tuning was adjusted slightly based on the driving cycle test SOC estimation, by varying the Q matrix with factors of ten.

6-4 RC Model

The RC model uses Equation 6-2 as its SOC-OCV relationship and has five states that were initialized as

$$\begin{aligned} x^+[0] &= \begin{pmatrix} z[0] & V_p[0] & R_0[0] & \tau[0] & R_1[0] \end{pmatrix}^\top \\ &= \begin{pmatrix} \text{SOC}_0 & 0 & 0.05 & 10 & 0.05 \end{pmatrix}^\top \end{aligned}$$

For the SOC, multiple simulations are run with different initial SOC conditions to assess the influence of the initial SOC error on algorithm performance. Therefore, $z[0]$ is replaced by SOC_0, which is set to 80%, 90%, and 100%. The polarization voltage is guessed at zero because at the beginning of the experiment, the cell should be in a relaxed depolarized state. $P^+[0]$ was tuned to

$$P^+[0] = \begin{pmatrix} (0.5/3)^2 & 0 & 0 & 0 & 0 \\ 0 & (0.2/3)^2 & 0 & 0 & 0 \\ 0 & 0 & (0.05/3)^2 & 0 & 0 \\ 0 & 0 & 0 & (10/3)^2 & 0 \\ 0 & 0 & 0 & 0 & (0.05/3)^2 \end{pmatrix}$$

Where the initial conditions for the parameters are used as the 3σ values to compute their initial state covariance. The SOC uncertainty uses a 0.5 value because this produced good results for all initial SOC conditions and that is the maximum $\pm$-range the SOC will have when guessing 50% SOC, exactly in the middle of the region. The polarization voltage uncertainty was set to 0.2 since the cell might not be fully depolarized from the charge phase when the dynamic profile experiment starts.

Lastly, Q was found to improve the algorithm performance when the process noise covariance of the polarization voltage was relatively high, and low for the other states, resulting in

$$Q = \begin{pmatrix} \text{1e-10} & 0 & 0 & 0 & 0 \\ 0 & \text{1e-5} & 0 & 0 & 0 \\ 0 & 0 & \text{1e-10} & 0 & 0 \\ 0 & 0 & 0 & \text{1e-10} & 0 \\ 0 & 0 & 0 & 0 & \text{1e-10} \end{pmatrix}$$

The improved performance with a high process noise on the polarization can be explained by the fact that a more realistic representation of the battery cell voltage response to current profiles is nonlinear, while in the RC model, the polarization is approximated by a single RC-pair with linear dynamics. A higher process noise thus gives the JUKF more freedom to adapt the polarization voltage.

6-4-1 Dynamic stress test

The JUKF RC model framework is first applied to the DST profile. The residuals between the JUKF and the measurements for the three different initial SOC conditions are shown

in Figure 6-13, where the residual voltage is in mV. The variance of the residuals is small in magnitude and the mean is close to zero, which shows that the algorithm converges to a solution quickly and is capable of following the measurements throughout the experiment. However, a deviation from zero-mean can be seen at the end of the experiment when the SOC is low, where the simple model struggles to represent the cell dynamics.

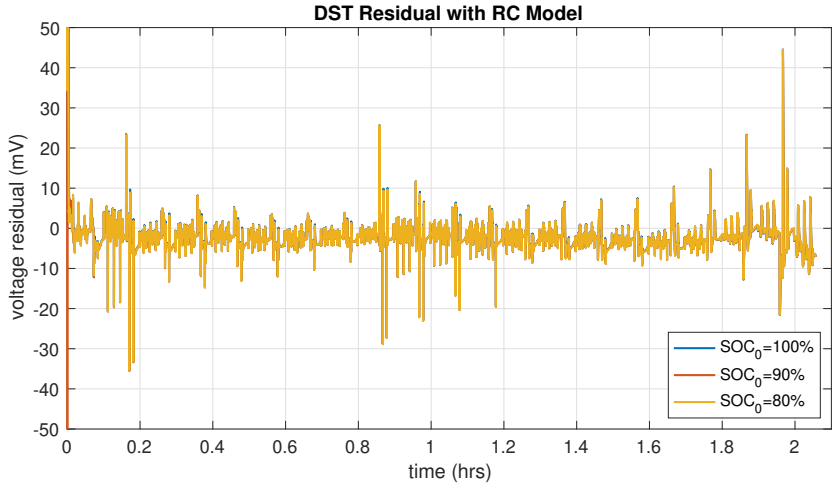

Figure 6-13: DST residual with the RC model.

Figure 6-14 and Figure 6-15 show the SOC estimation and the estimation error using the RC model. Initially, All starting conditions are able to converge to similar estimates of the baseline SOC, within about 0.5%, but the estimations drift as the SOC decreases and eventually end at about 2% error at the end of the DST.

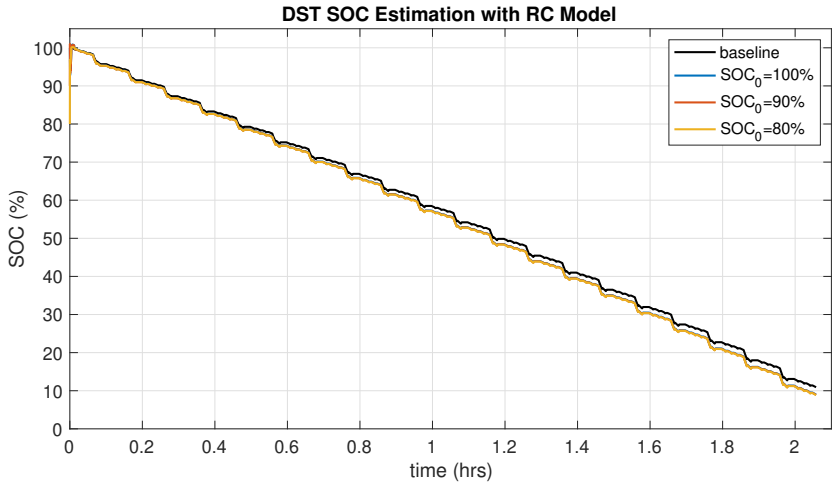

Figure 6-14: DST SOC estimation with the RC model.

Lastly, the ohmic resistance estimated by the JUKF is shown in Figure 6-16, which confirms that the resistance is not constant but varies between roughly 35 to 43 mΩ, depending on the state-of-charge. All three initial SOCs converge to roughly the same resistance values,

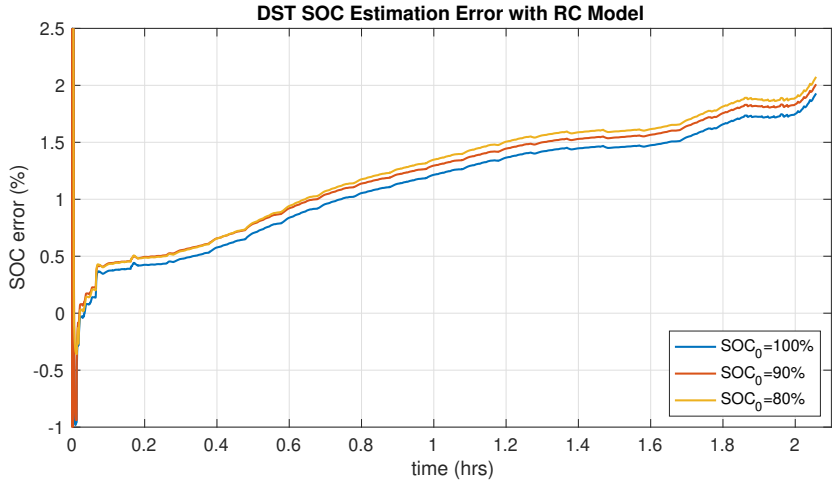

Figure 6-15: DST SOC estimation error with the RC model.

indicating that the ohmic resistance estimation is largely independent of the initial conditions.

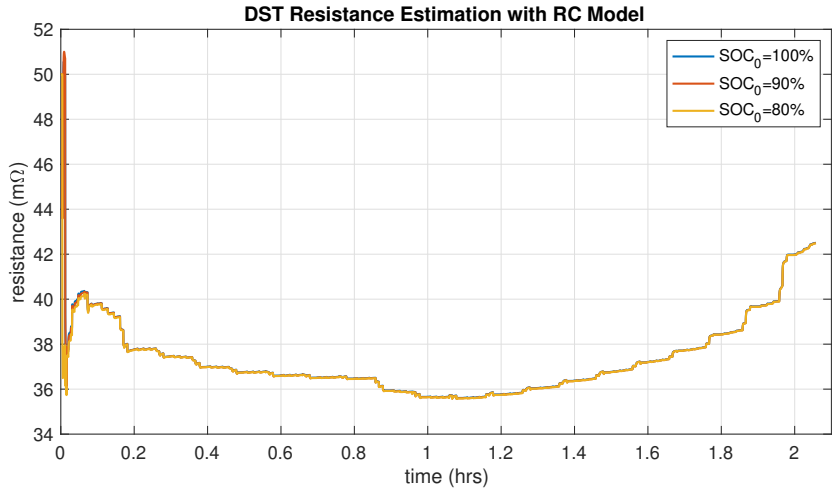

Figure 6-16: DST resistance estimation with the RC model.

6-4-2 Driving cycle test

The RC model framework is now run on the DCT profile. The residuals are plotted in Figure 6-17. In comparison with the DST results, these residuals show more variance and higher frequency due to the more complex profile. Similarly to the DST, the residual deviates significantly from the mean at the lower SOC range.

Figure 6-18 and Figure 6-19 plot the SOC estimation and the estimation error of the DCT over time. Compared to the DST results, these plots show a similar drift of the SOC estimation over time, but the magnitude of the error is larger in the DCT and at low SOC the baseline SOC is underestimated by almost 6%.

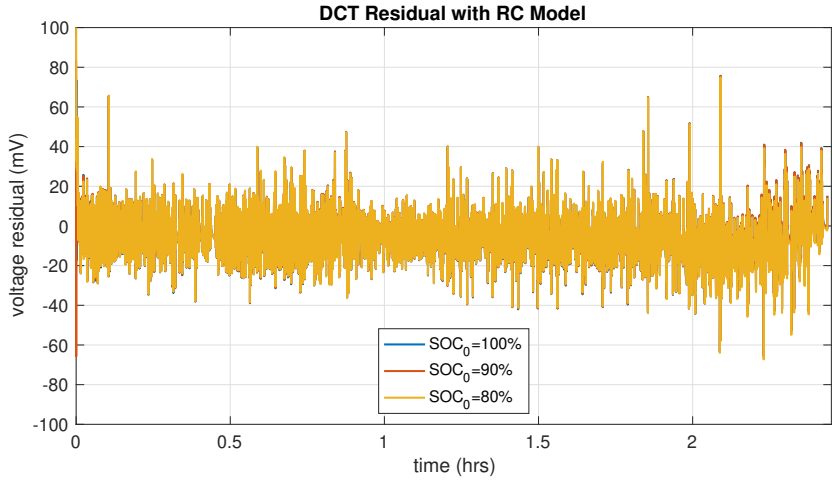

Figure 6-17: DCT residual with the RC model.

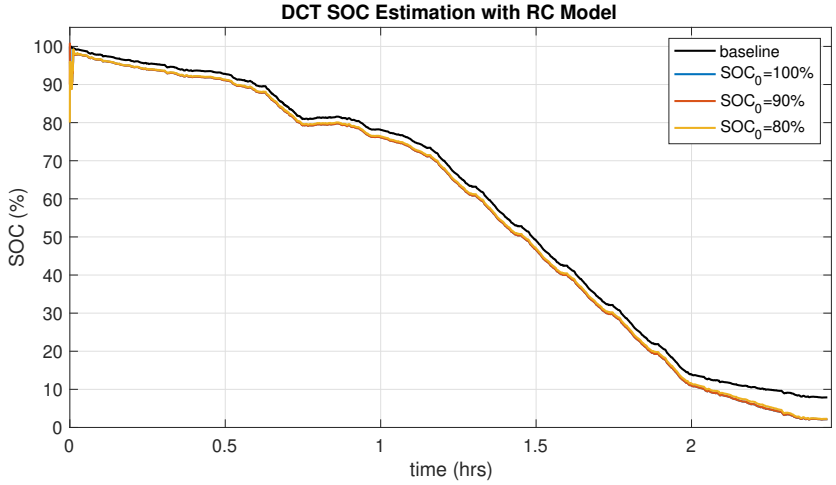

Figure 6-18: DCT SOC estimation with the RC model.

The estimated ohmic resistance can be plotted for the DCT as well, which is shown in Figure 6-20. The estimation again varies with SOC and the three initial conditions converge to very similar resistance values. The overall DCT estimation converges to smaller resistance values than the DST resistance. While both tests end at roughly 10% SOC, the DST ohmic resistance reaches almost 43 mΩ, while the DCT estimation stops at 38 mΩ. This can likely be attributed to different internal temperatures that influence the ohmic resistance.

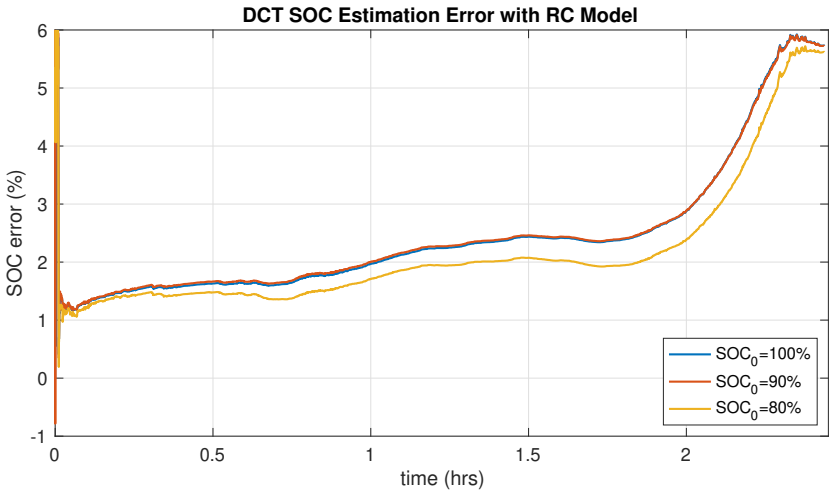

Figure 6-19: DCT SOC estimation error with the RC model.

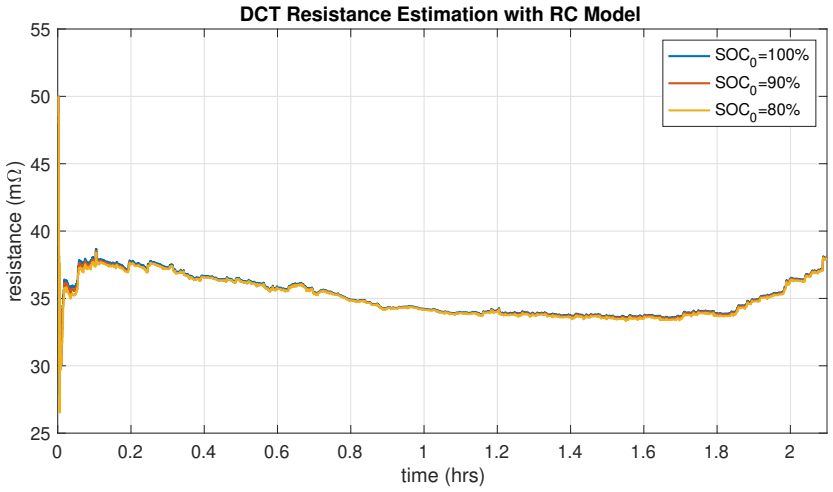

Figure 6-20: DCT resistance estimation with the RC model.

6-5 RC-Hysteresis Model

The RC-H model again uses Equation 6-2 as its SOC-OCV relationship and includes three additional states to the joint state vector, the hysteresis voltage, the hysteresis rate, and the maximum hysteresis. The initial guess is given by

$$\begin{aligned} x^+[0] &= \begin{pmatrix} z[0] & V_p[0] & V_h[0] & R_0[0] & \tau[0] & R_1[0] & \gamma[0] & M[0] \end{pmatrix}^\top \\ &= \begin{pmatrix} \text{SOC}_0 & 0 & 0 & 0.05 & 10 & 0.05 & \text{1e-3} & 0.1 \end{pmatrix}^\top \end{aligned}$$

For the initial state uncertainty, the initial hysteresis uncertainty was determined from typical hysteresis values seen in the low-current voltage data. The hysteresis rate was more difficult and had to be tuned iteratively to find a suitable order of magnitude. The initial voltage hysteresis was set to zero, which produced reasonable results, although the hysteresis is expected to be larger than zero because at the start the cell is recovering from a charge phase. Other values are identical to the RC model tuning. $P^+[0]$ is tuned in the same way as for the RC model with the addition of three more variances on its diagonal due to the increase in states,

$$P^+[0] = \begin{pmatrix} (0.5/3)^2 & 0 & 0 & 0 & 0 & 0 & 0 & 0 \\ 0 & (0.2/3)^2 & 0 & 0 & 0 & 0 & 0 & 0 \\ 0 & 0 & (0.1/3)^2 & 0 & 0 & 0 & 0 & 0 \\ 0 & 0 & 0 & (0.05/3)^2 & 0 & 0 & 0 & 0 \\ 0 & 0 & 0 & 0 & (10/3)^2 & 0 & 0 & 0 \\ 0 & 0 & 0 & 0 & 0 & (0.05/3)^2 & 0 & 0 \\ 0 & 0 & 0 & 0 & 0 & 0 & (\text{1e-3}/3)^2 & 0 \\ 0 & 0 & 0 & 0 & 0 & 0 & 0 & (0.1/3)^2 \end{pmatrix}$$

In the third entry on the diagonal, the initial uncertainty in the voltage hysteresis is set by the expected maximum hysteresis. Q is again very similar to the RC model tuning,

$$Q = \begin{pmatrix} \text{1e-10} & 0 & 0 & 0 & 0 & 0 & 0 & 0 \\ 0 & \text{1e-5} & 0 & 0 & 0 & 0 & 0 & 0 \\ 0 & 0 & \text{1e-9} & 0 & 0 & 0 & 0 & 0 \\ 0 & 0 & 0 & \text{1e-10} & 0 & 0 & 0 & 0 \\ 0 & 0 & 0 & 0 & \text{1e-10} & 0 & 0 & 0 \\ 0 & 0 & 0 & 0 & 0 & \text{1e-10} & 0 & 0 \\ 0 & 0 & 0 & 0 & 0 & 0 & \text{1e-10} & 0 \\ 0 & 0 & 0 & 0 & 0 & 0 & 0 & \text{1e-10} \end{pmatrix}$$

Hysteresis process noise is included to reflect the fact that the hysteresis model is a simplification of the actual voltage hysteresis.

6-5-1 Dynamic stress test

Replacing the RC model with the RC-H model and using the dynamic stress test data results in the residuals shown in Figure 6-21. Although the RC-H model has three extra states, the

residuals show that it is still able to converge to a suitable solution fairly quickly. The residual mean is close to zero for most of the time, but also still struggles with the lower SOC region. In comparison to the RC model DST residual, Figure 6-13, the mean of the RC-H residual is closer to zero, as the addition of hysteresis increases the model complexity and thus reduces the overall model bias.

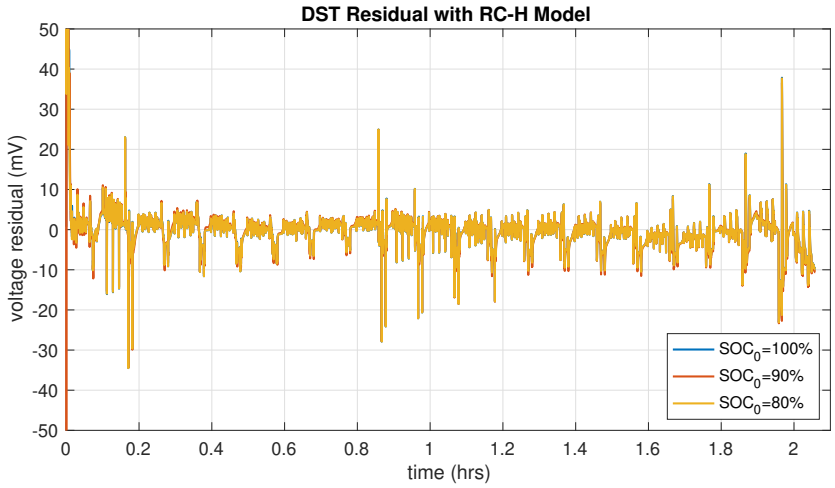

Figure 6-21: DST residual with the RC-H model.

The SOC estimation and estimation error plots, in Figure 6-22 and Figure 6-23, show that the SOC estimation benefits greatly from the additional model complexity. The SOC drift is mostly eliminated and the error stays within about 0.5% SOC for all three initial conditions. The largest errors can be seen at low SOC just before the test ends.

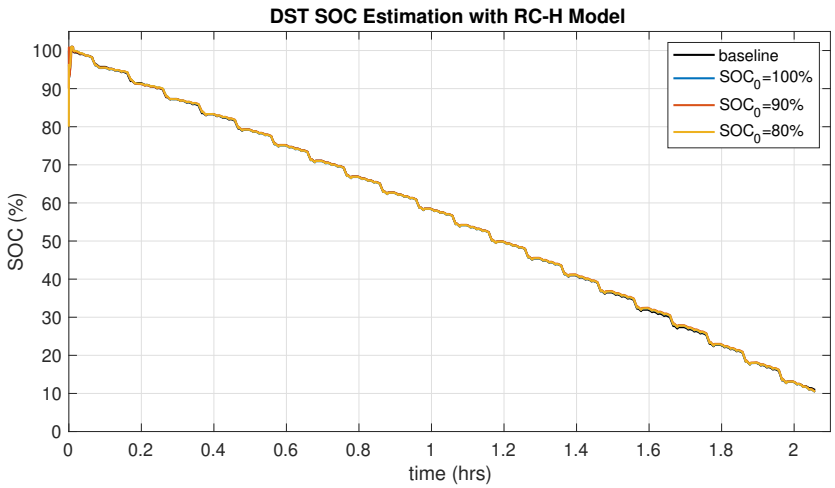

Figure 6-22: DST SOC estimation with the RC-H model.

Figure 6-24 displays the estimation of the voltage hysteresis in the RC-H model for the multiple initial conditions. All three initial conditions converge to almost identical values. The estimated hysteresis starts out as slightly positive but then switches signs and stays

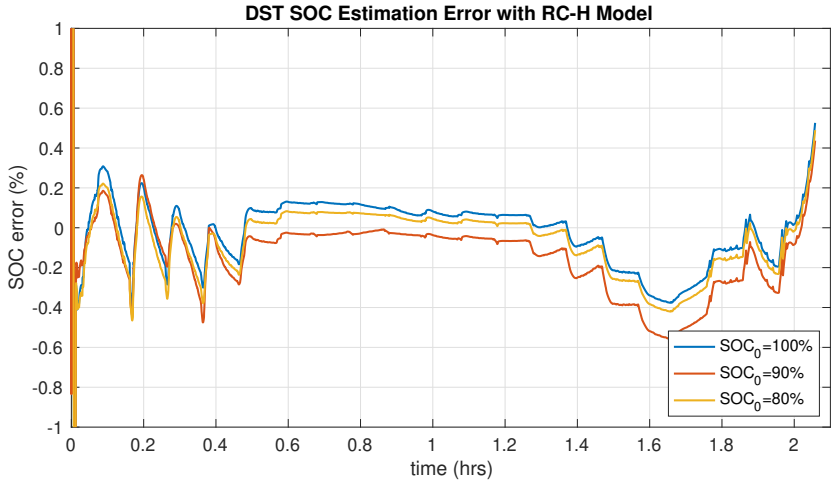

Figure 6-23: DST SOC estimation error with the RC-H model.

negative for the entire DST, as expected during a discharge profile. The hysteresis is highest near the end of the test, at low SOC.

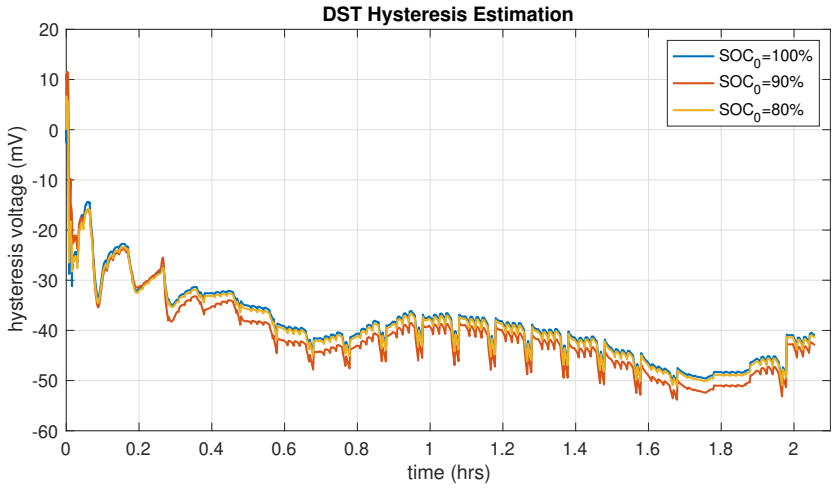

Figure 6-24: DST hysteresis estimation with the RC-H model.

The RC-H resistance estimation is shown in Figure 6-25. It can be seen that the estimation has the same pattern and converges to similar values when compared to the RC DST estimation.

6-5-2 Driving cycle test

Figure 6-26 shows the residual of the RC-H JUKF framework on the DCT profile, which again is close to zero-mean and similar to the residual of the RC model on the DCT data.

Figure 6-27 and Figure 6-28 display the results of the SOC estimation during the driving cycle test. After a convergence period, the 100% and 90% initial conditions produce an almost $\pm 1\%$

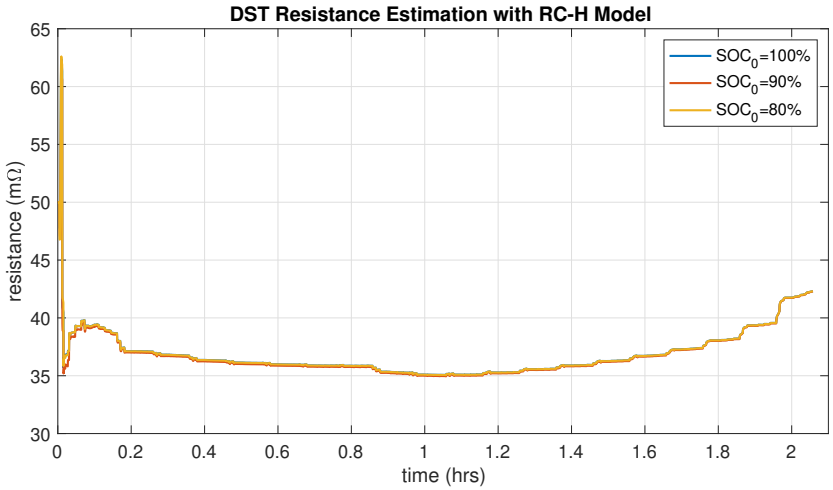

Figure 6-25: DST resistance estimation with the RC-H model.

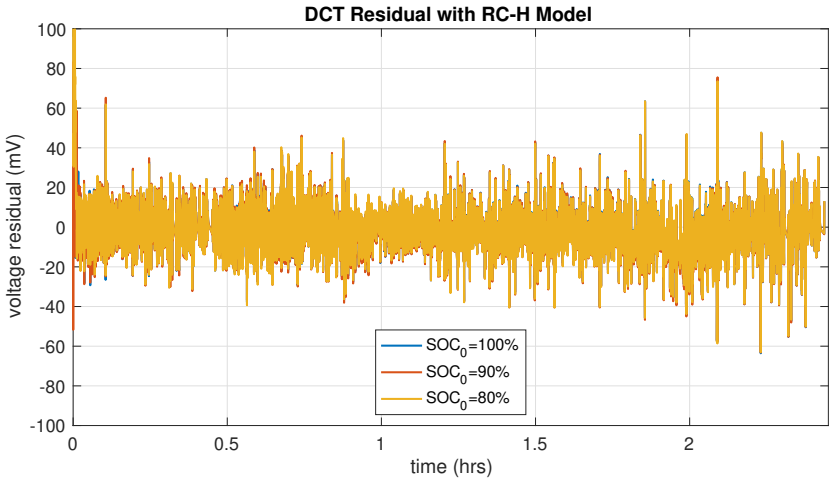

Figure 6-26: DCT residual with the RC-H model.

accurate SOC estimation. The estimation pattern when using SOC_0=80% differs greatly from 100% and 90%, especially in the first half of the test.

The estimated hysteresis voltage is shown in Figure 6-24. The three initial conditions converge to similar hysteresis values, and the hysteresis is highest at low SOC. Interestingly, the DCT hysteresis is larger than the DST hysteresis, especially at low SOC when the DCT hysteresis increases rapidly.

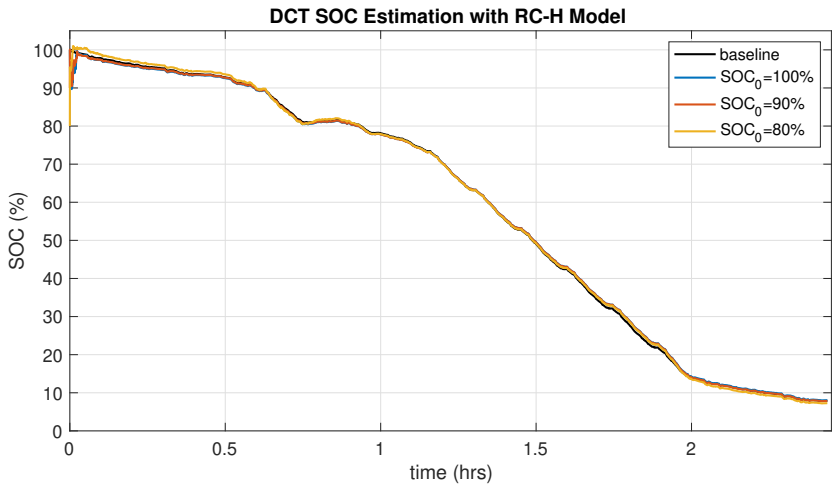

Figure 6-27: DCT SOC estimation with the RC-H model.

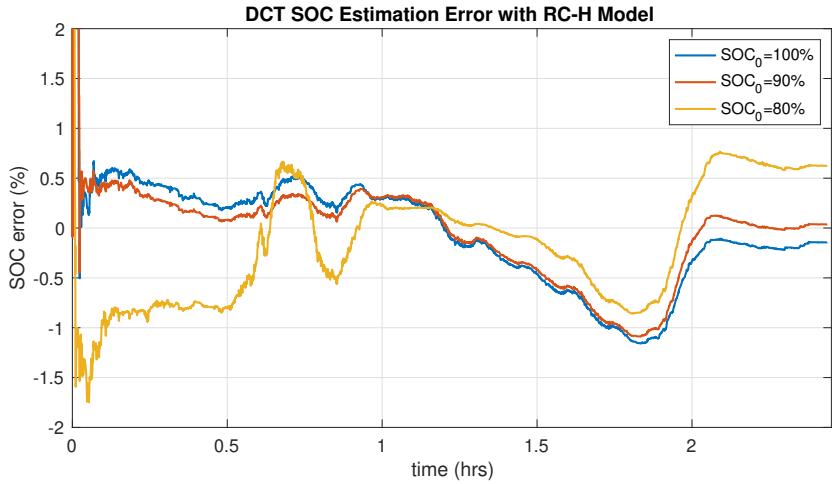

Figure 6-28: DCT SOC estimation error with the RC-H model.

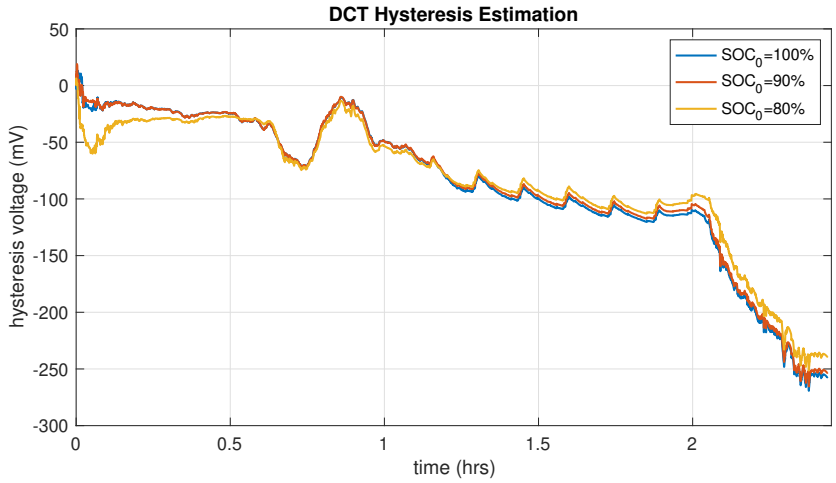

Figure 6-29: DCT hysteresis estimation with the RC-H model.

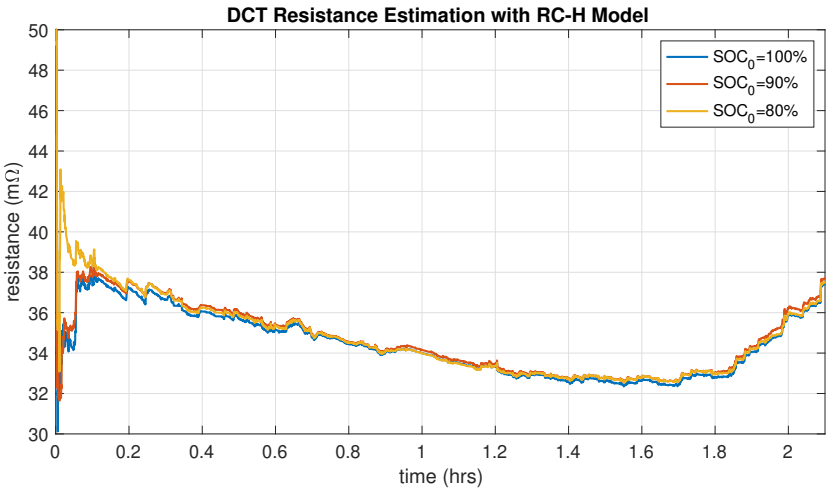

Figure 6-30: DCT resistance estimation with the RC-H model.

6-6 Adaptive-RC-Hysteresis Model

The replacement of the OCV function with an affine relationship drastically changed the performance of the JUKF and required partial retuning. The first challenge is to pick reasonable initial values for the coefficients c_0 and c_1. Using a priori knowledge of this cell's chemistry and insights from Section 6-1, the SOC-OCV curve has a wide region between 10% to 100% SOC where the trend is reasonably linear. A rough trendline through this region can approximate the SOC-OCV relationship with OCV $= 3.3 + 0.9z$, meaning $c_0 = 3.3$ and $c_1 = 0.9$. These values are used as initial conditions for the JUKF, turning the initial state vector into

$$\begin{aligned} x^+[0] &= \begin{pmatrix} z[0] & V_p[0] & V_h[0] & R_0[0] & \tau[0] & R_1[0] & \gamma[0] & M[0] & c_0[0] & c_1[0] \end{pmatrix}^\top \\ &= \begin{pmatrix} \mathrm{SOC}_0 & 0 & 0 & 0.05 & 10 & 0.05 & \text{1e-3} & 0.1 & 3.3 & 0.9 \end{pmatrix}^\top \end{aligned}$$

The state uncertainty covariance matrix is purposely kept similar to the RC-H model's $P^+[0]$, with the addition of uncertainty in the affine function parameters,

$$P^+[0] = \begin{pmatrix} (0.5/3)^2 & 0 & 0 & 0 & 0 & 0 & 0 & 0 & 0 & 0 \\ 0 & (0.2/3)^2 & 0 & 0 & 0 & 0 & 0 & 0 & 0 & 0 \\ 0 & 0 & (0.1/3)^2 & 0 & 0 & 0 & 0 & 0 & 0 & 0 \\ 0 & 0 & 0 & (0.05/3)^2 & 0 & 0 & 0 & 0 & 0 & 0 \\ 0 & 0 & 0 & 0 & (10/3)^2 & 0 & 0 & 0 & 0 & 0 \\ 0 & 0 & 0 & 0 & 0 & (0.05/3)^2 & 0 & 0 & 0 & 0 \\ 0 & 0 & 0 & 0 & 0 & 0 & (\text{1e-3}/3)^2 & 0 & 0 & 0 \\ 0 & 0 & 0 & 0 & 0 & 0 & 0 & (0.1/3)^2 & 0 & 0 \\ 0 & 0 & 0 & 0 & 0 & 0 & 0 & 0 & (0.1/3)^2 & 0 \\ 0 & 0 & 0 & 0 & 0 & 0 & 0 & 0 & 0 & (0.1/3)^2 \end{pmatrix}$$

The process noise covariance matrix is given by,

$$Q = \begin{pmatrix} \text{1e-10} & 0 & 0 & 0 & 0 & 0 & 0 & 0 & 0 & 0 \\ 0 & \text{1e-3} & 0 & 0 & 0 & 0 & 0 & 0 & 0 & 0 \\ 0 & 0 & \text{1e-5} & 0 & 0 & 0 & 0 & 0 & 0 & 0 \\ 0 & 0 & 0 & \text{1e-10} & 0 & 0 & 0 & 0 & 0 & 0 \\ 0 & 0 & 0 & 0 & \text{1e-10} & 0 & 0 & 0 & 0 & 0 \\ 0 & 0 & 0 & 0 & 0 & \text{1e-10} & 0 & 0 & 0 & 0 \\ 0 & 0 & 0 & 0 & 0 & 0 & \text{1e-10} & 0 & 0 & 0 \\ 0 & 0 & 0 & 0 & 0 & 0 & 0 & \text{1e-10} & 0 & 0 \\ 0 & 0 & 0 & 0 & 0 & 0 & 0 & 0 & \text{1e-10} & 0 \\ 0 & 0 & 0 & 0 & 0 & 0 & 0 & 0 & 0 & \text{1e-10} \end{pmatrix}$$

The biggest change is an increased process noise for the polarization and the hysteresis voltage. For both coefficients, the process noise was set to 1e-10.

The measurement noise covariance had to be increased to $R = 0.1$, to improve estimation performance. This is likely caused by the increased error in the model due to the replacement of the high-order polynomial SOC-OCV function with a heavily simplified affine function.

6-6-1 Dynamic stress test

The DST SOC estimation and the error between the baseline and the estimation using the A-RC-H model are displayed in Figure 6-31 and Figure 6-32. The results show that the performance is heavily influenced by the initial SOC guess. When the guess is correct, the SOC error is within ±1.5% for the entire SOC range, but at SOC_0=80% the error increases to between 2.5% and 4%.

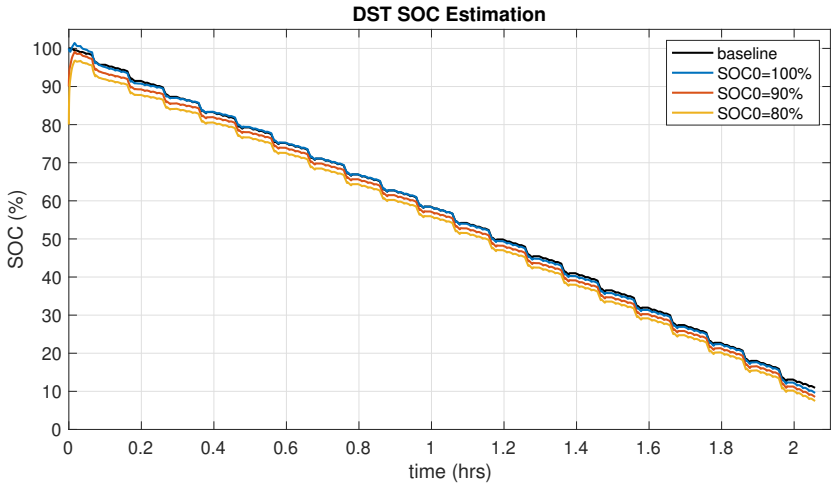

Figure 6-31: DST SOC estimation with the A-RC-H model.

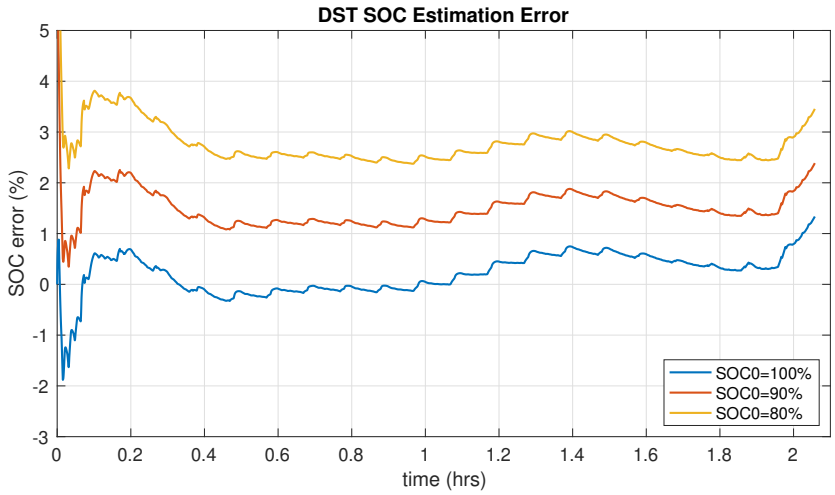

Figure 6-32: DST SOC estimation error with the A-RC-H model.

The implicit OCV estimation can be reconstructed by computing $c_0 + c_1 z$ using the state estimates at every time step, resulting in Figure 6-33. The plot shows the estimation compared with the baseline SOC-OCV curve, calculated from the SOC baseline values, plugged into the OCV polynomial function found in Section 6-1. The figure shows that the OCV estimation can capture the overall downward trend of the SOC-OCV relationship, but mostly struggles with the high and low SOC regions. Interestingly, a better approximation of the OCV does not

seem to correlate with a better SOC estimation, as the SOC_0=80% and SOC_0=90% appear to be closer to the actual OCV than the 100% initial guess. This can likely be attributed to the non-uniqueness of the estimations in Kalman filters, where the convergence to actual values is not guaranteed.

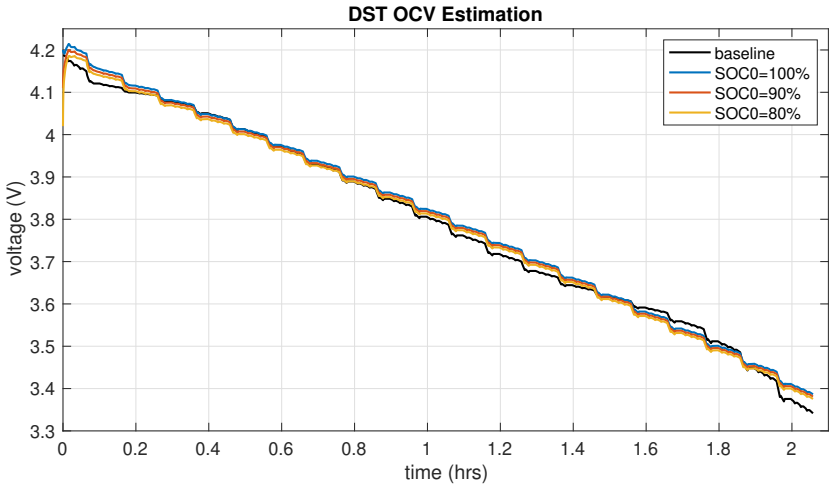

Figure 6-33: DST OCV estimation with the A-RC-H model.

6-6-2 Driving cycle test

Figure 6-34, and Figure 6-35 display the residual, SOC estimation, and SOC estimation error for the DCT using three different initial conditions. The DCT residuals follow a familiar pattern, oscillating around 0 mV until about 2 hours into the test, where the SOC is low. The SOC estimation again shows the correlation between the initial guess and the SOC error. In the DCT, the error is amplified at low SOC, resulting in a maximum error of about 7% when using an initial SOC of 80%. When the guess is correct, the error stays below 2% for most of the SOC range but jumps to about 4% after the 20% SOC point.

Finally, the implicit OCV estimation can be derived from the estimations of c_0 and c_1, yielding Figure 6-36. The OCV is initially overestimated and fails to capture the low SOC behavior after about 1.7 hrs into the test, but the estimation still captures the main decreasing trend.

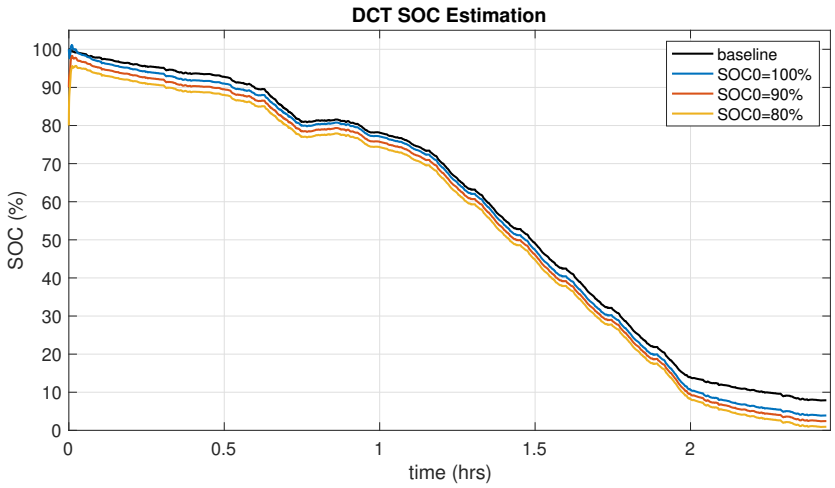

Figure 6-34: DCT SOC estimation with the A-RC-H model.

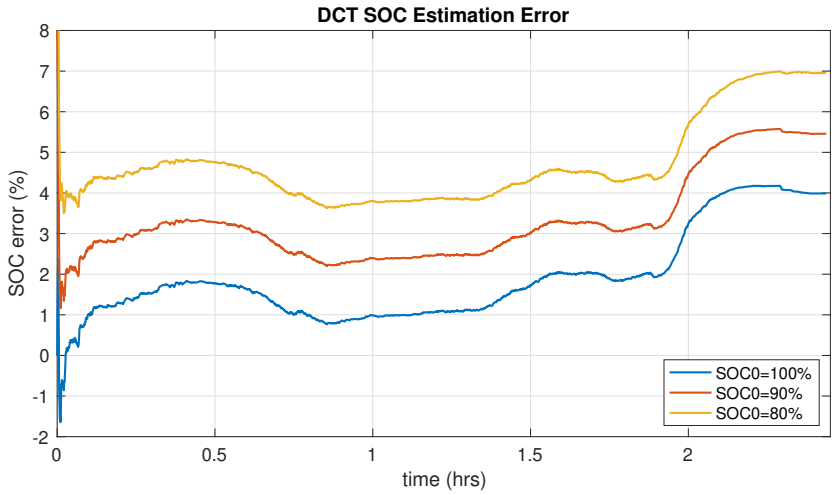

Figure 6-35: DCT SOC estimation error with the A-RC-H model.

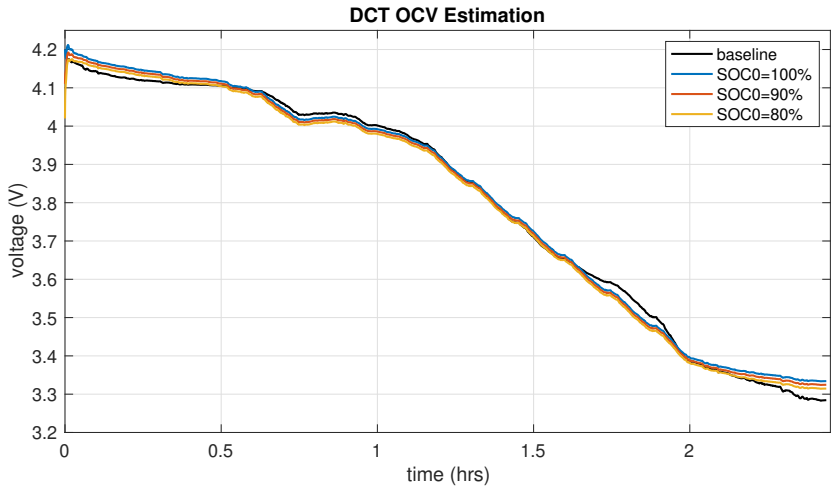

Figure 6-36: DCT OCV estimation with the A-RC-H model.

6-7 Analysis of the Results

The SOC estimation results from each model are benchmarked using three performance metrics, root-mean-square error (RMSE), mean-absolute error (MAE), and max-absolute error (MAXAE). The RMSE was defined in Equation 6-1. MAE is the normalized 1-norm,

$$\text{MAE} = \frac{1}{N}\sum_{i=0}^{N}|e_i| \tag{6-4}$$

and MAXAE is the ∞-norm,

$$\text{MAXAE} = \max|e_i| \tag{6-5}$$

The MAXAE is computed over the SOC errors after the approximate convergence of the SOC. Otherwise, the max SOC error with an initial condition of 80% would always be 20%, which is not a meaningful performance metric.

6-7-1 Dynamic stress test

Figure 6-37, Figure 6-38, and Figure 6-39 display the evaluation of the SOC estimation at 100%, 90%, and 80% SOC_0 during the DST profile. The results show that the RC-H model outperforms the RC and A-RC-H models. The second observation to make is, while the RC and RC-H estimations are fairly insensitive to initial SOC, the A-RC-H performance is highly dependent on the initial guess, with larger initial errors resulting in much higher RMSE, MAE, and MAXAE values. At SOC_0=100%, the RMSE and MAE values of the A-RC-H model show similar performance compared to the RC-H model, but the MAXAE value is larger and on par with the RC model.

The last thing to point out is that, for the RC and RC-H models, a lower initial SOC error does not guarantee a better model performance. This can be attributed to the initial SOC uncertainty, which is kept constant for all initial conditions. When the filter is initialized at the ground truth of 100%, the high uncertainty means that the filter does not immediately converge to 100% SOC but instead allows all parameters to vary according to their uncertainty ranges to make the residual converge to minimum variance.

6-7-2 Driving cycle test

The analysis process is repeated for the driving cycle test, resulting in Figure 6-40, Figure 6-41, and Figure 6-42. The DCT results parallel the DST graphs but with larger values due to the increased difficulty of estimating SOC from the more complex dynamic profile. In this case, an SOC_0 of 80% actually produces the best performance for the RC model, and SOC_0=90% for the RC-H model. Compared to the DST, the maximum error of the RC-H model during the DCT seems to be more affected by the initial guess. With SOC_0=80% the maximum error increases by about 50% compared to SOC_0=100% and SOC_0=90%.

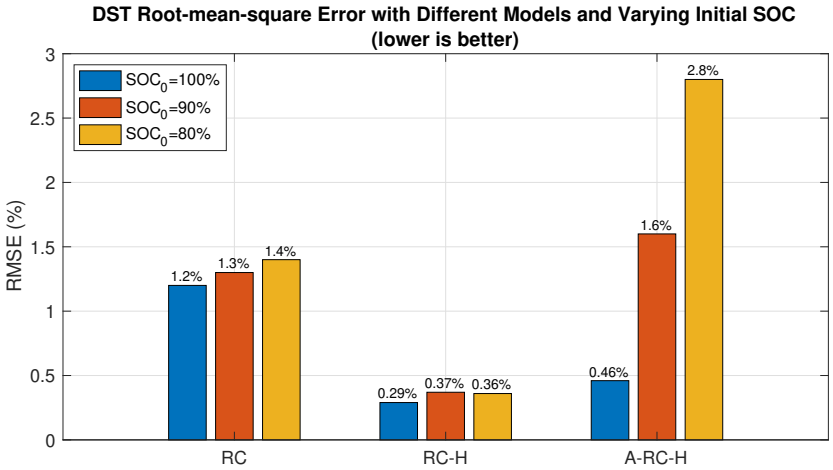

Figure 6-37: DST RMSE with different models and varying initial SOC.

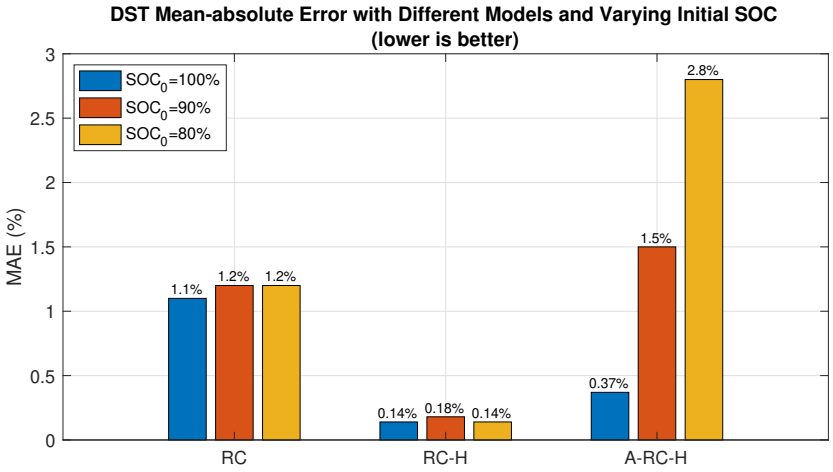

Figure 6-38: DST MAE with different models and varying initial SOC.

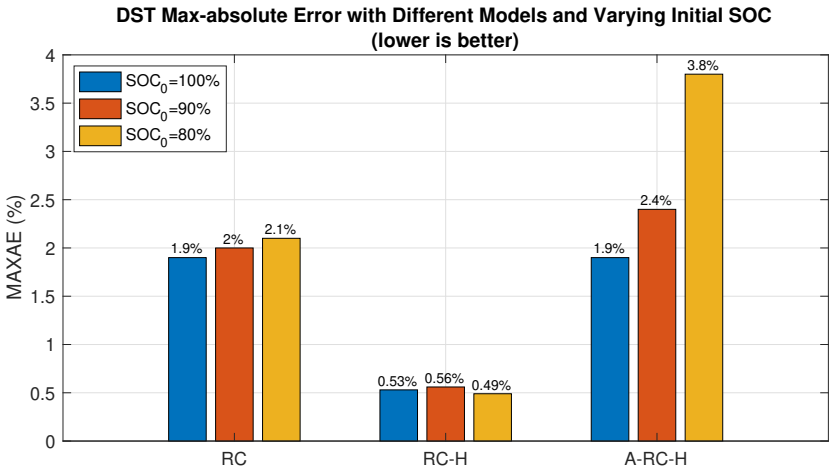

Figure 6-39: DST MAXAE with different models and varying initial SOC.

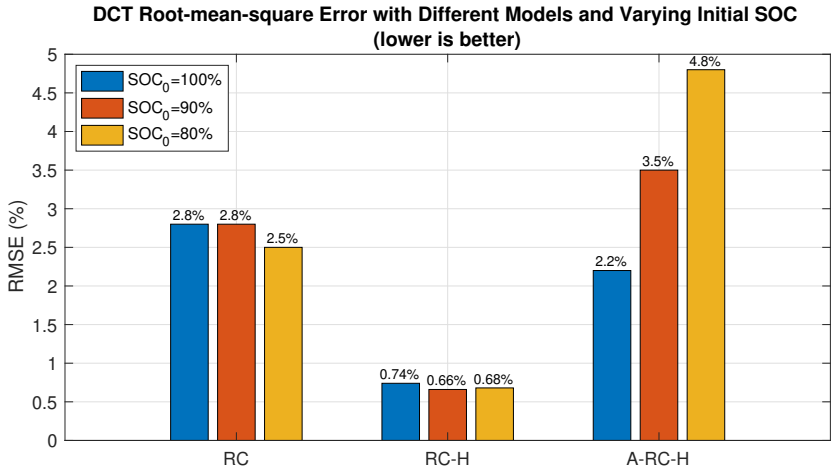

Figure 6-40: DCT RMSE with different models and varying initial SOC.

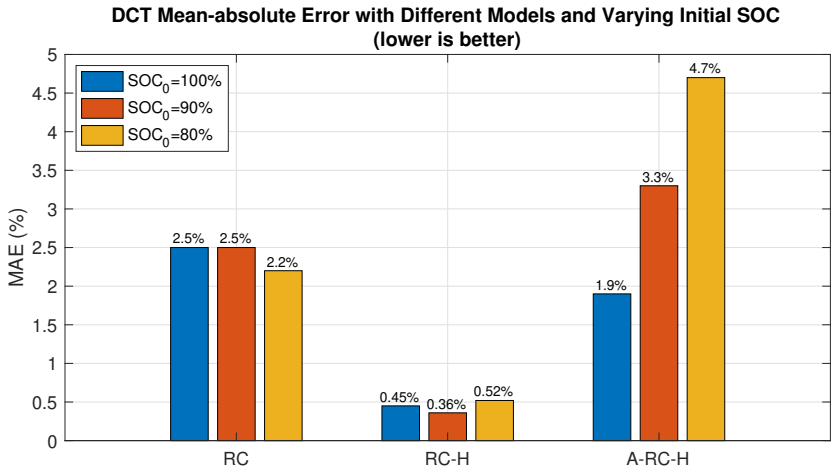

Figure 6-41: DCT MAE with different models and varying initial SOC.

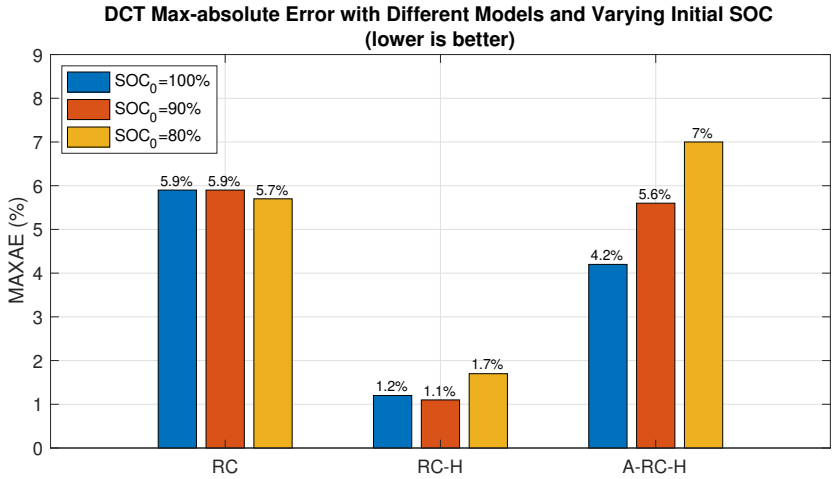

Figure 6-42: DCT MAXAE with different models and varying initial SOC.

6-8 Aging Effects

As the cell ages, total capacity decreases, ohmic resistance increases, and the SOC-OCV relationship drifts. To investigate and validate the capability of the model to estimate the rising resistance and the effects of capacity fade and OCV drift on the SOC estimation, the remaining three dynamic stress tests, at different SOH_C stages, are used as data for the three model frameworks. The JUKF tuning parameters were unchanged from their begin-of-life values.

The time it takes to run the DST profile decreases as the cell ages because the minimum voltage is reached faster due to higher ohmic losses and decreased capacity.

6-8-1 Ohmic resistance

The ohmic losses are proportional to the ohmic resistance, one of the parameters being estimated by the JUKF. To see the evolution of the ohmic losses over the SOH_C, the estimated ohmic resistance during each DST is shown in Figure 6-43. The results verify that the resistance increases during the cell's lifetime, almost doubling at 70% SOH_C versus begin-of-life.

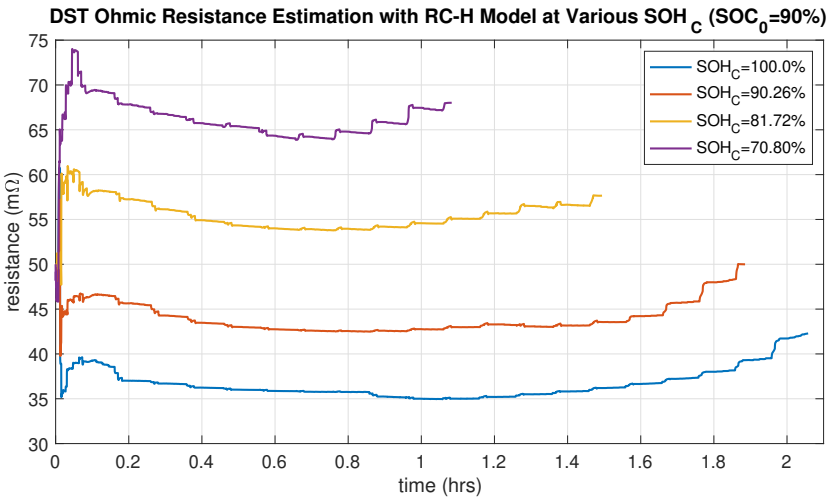

Figure 6-43: DST resistance estimation with RC-H model at various SOH_C (SOC_0=90%)

6-8-2 SOC estimation

To visualize the progression of the SOC estimation over the SOH_C, the estimation error is plotted for each DST in Figure 6-44, using the RC-H model and an initial SOC of 90%. This shows that the error tends to increase with state-of-health, which can be explained by the SOC-OCV drift but could also be a consequence of the fact that the Kalman filter is tuned based on BOL performance.

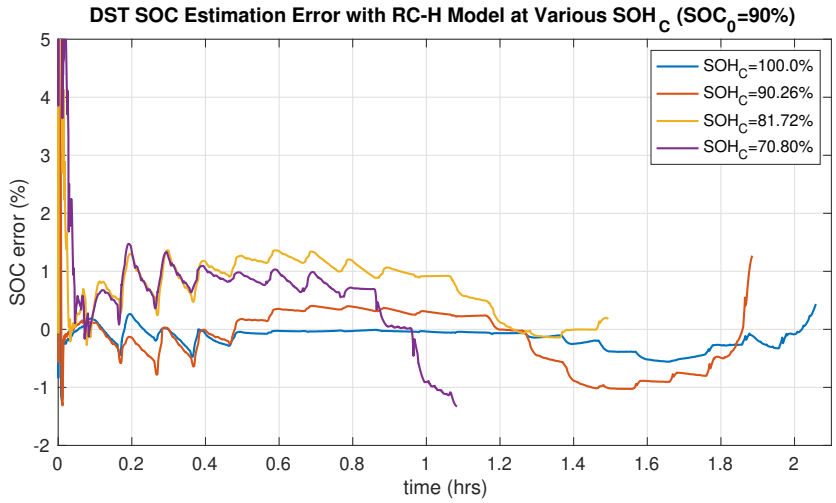

Figure 6-44: DST SOC estimation error with RC-H model at various SOH_C (SOC_0=90%)

6-8-3 Analysis

The SOC estimation performance can be quantified and analyzed by applying the same analysis process from Section 6-7 on the fourth and last dynamic stress test, with SOH_C ≈70. The resulting RMSE, MAE, and MAXAE values using different initial conditions are plotted in Figure 6-45, Figure 6-46, and Figure 6-47.

The results show that overall errors are larger at $SOH_C \approx 70$, but most of the conclusions from Section 6-7 are valid here as well. The RC model is mostly independent of the initial SOC guess, while the A-RC-H model is highly sensitive to the initial SOC, as all metrics almost double in magnitude between 100% and 80%.

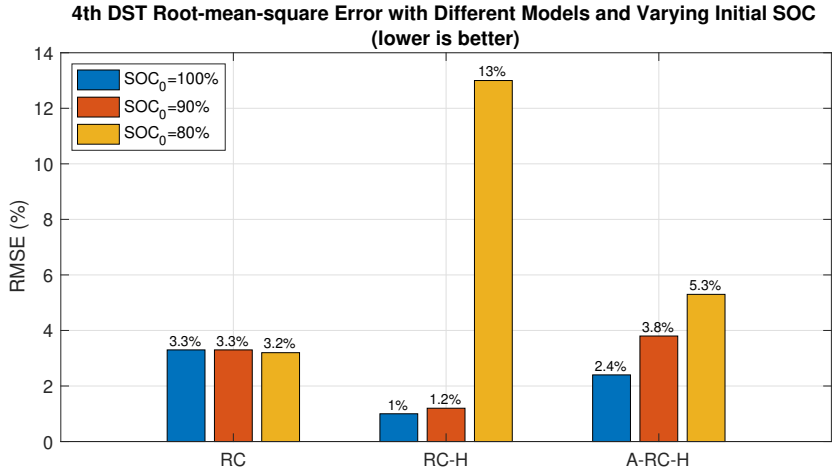

Figure 6-45: 4th DST RMSE with different models and varying initial SOC.

With SOC_0=100% and SOC_0=90%, the performance of the RC-H model is still superior to the other two models, but a spike in RMSE, MAE, and MAXAE can be observed at 80% SOC_0. The RC-H SOC estimation error versus time for the fourth DST is plotted in Figure 6-48. It can be seen that the spike in performance at 80% SOC_0 is due to the JUKF converging

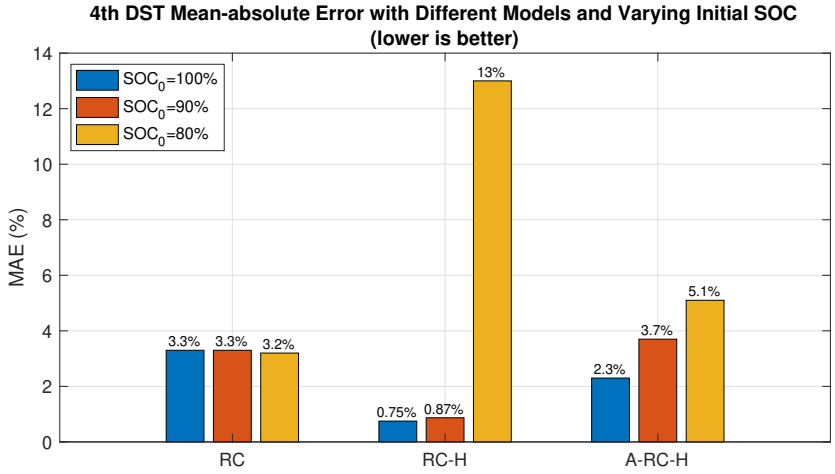

Figure 6-46: 4th DST MAE with different models and varying initial SOC.

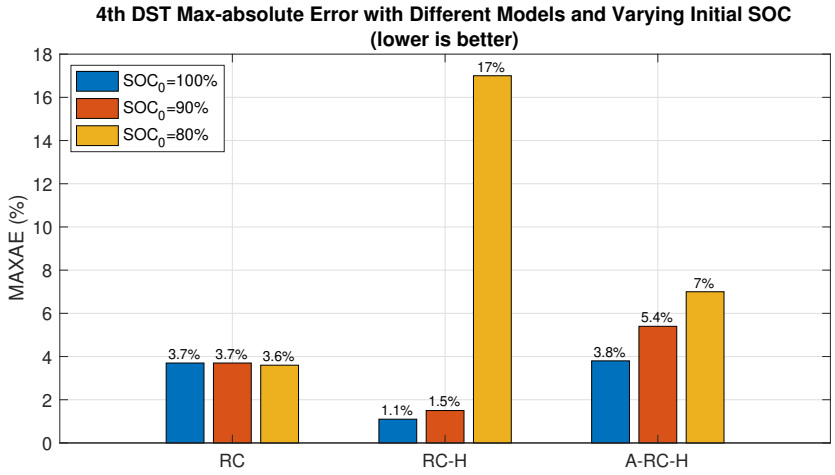

Figure 6-47: 4th DST MAXAE with different models and varying initial SOC.

to much lower values for the entire duration of the DST profile, which greatly underestimates the SOC. With smaller SOC errors, the estimation converges normally to values close to the baseline. The spike can be prevented by retuning the JUKF, but it was chosen not to do this to preserve the idea that the aged data is 'unseen' data.

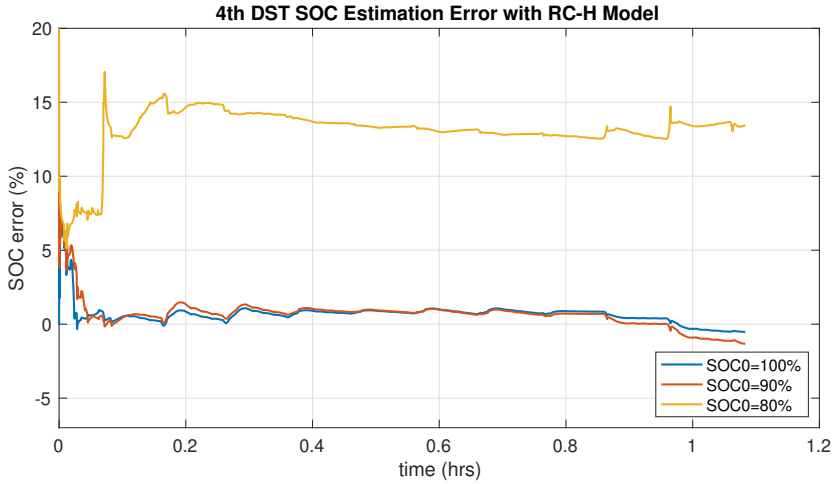

Figure 6-48: 4th DST SOC estimation error with RC-H model.

Chapter 7

Conclusion

The objective of this work was to explore the use of hysteresis models to improve SOC estimations in NMC/Si-C lithium-ion cell chemistries and to investigate whether time-consuming SOC-OCV tests can be replaced by an online estimation of the OCV. The SOC estimation tests were run at three different initial SOC guesses and with three different battery cell models, the RC, RC-Hysteresis, and A-RC-H models.

The results show that the RC-Hysteresis model produces superior SOC estimations compared to RC model, reducing driving cycle test RMSE from at most 2.8% to only 0.74% and driving cycle test MAXAE from at most 5.9% to 1.7%. However, the model is less robust to large initial SOC errors when the cell has aged significantly. The RC model leads to higher SOC errors, but is largely insensitive to the initial SOC error and has reduced computational complexity due to its smaller joint state vector. The SOC errors are typically highest in the low SOC region, which coincides with where the voltage hysteresis is highest and where the fitted SOC-OCV polynomial has the largest error.

Lastly, the estimation results of the A-RC-H show that the model is capable of reconstructing the main trend in OCV. However, the simplified SOC-OCV representation fails at capturing the more nonlinear portions of the curve, which often results in large errors at low SOC where the SOC-OCV trend is significantly different from the mid to high region. The overall SOC estimates are similar to the RC model performance, but the A-RC-H model is highly dependent on the initial SOC value, and lower initial errors always produce better results.

In conclusion, a single RC-pair battery model that includes voltage hysteresis vastly improves SOC estimation performance versus the no-hysteresis model and should be used for maximum SOC accuracy. However, this comes at the cost of additional complexity and lower robustness to initial conditions. More accurate SOC estimations have a trickle-down effect, where the accuracy of energy and capacity estimations are also improved, assuming the capacity is estimated with SOC-based methods, meaning the range and the end-of-life conditions for an electric vehicle can be assessed more accurately. This can effectively extend battery life and support decision-making concerning battery repurposing.

Meanwhile, the A-RC-H model produces reasonable SOC estimations and can reconstruct the main OCV trend. Though, the RMSE and MAE performance is only close to the RC model

when the initial SOC error is small. Practical implementation of the A-RC-H model could be viable if time-consuming and expensive SOC-OCV experiments are undesirable and the additional model complexity and higher SOC error are tolerable.

7-1 Discussion

The first discussion point concerns the accuracy of the SOC-OCV relationship. A portion of the accuracy of the SOC estimation depends on the correct measurement of the total capacity and the SOC-OCV relationship. It should be noted that, although a C/20 rate with a 1-hour resting time was used to compute the total capacity and SOC-OCV, the recommended setting is a C/30 test with a 2-hour resting period [1]. The experiment is a trade-off between time and accuracy and the EVERLASTING data set chose a quicker experiment that results in a slightly less accurate SOC-OCV and total capacity estimate. It has also been argued that SOC-OCV estimations from an incremental-current test produce better SOC results than the low-current test [36]. However, incremental tests were not part of the data set.

A second source of error in both parameter and SOC estimations could be the use of interpolation to transform the data into a consistently-spaced grid. Because of the variable time step in the original data, interpolation will create data points in some parts and decimate points at other locations. This consistent grid is easier to work with but creates a modified data set that is expected to be a slightly worse representation of the system than the actual measurements.

A third point of discussion is the tuning of the JUKF. Due to the many states and parameters involved, the tuning of $x^+[0]$, $P^+[0]$, Q, and R had a considerable impact on SOC estimation. This was tackled by approaching the tuning in a more structured way and by limiting the tuning of Q and R to factors of 10. This means that not all settings were tried and there could be different $x^+[0]$, $P^+[0]$, Q, and R values for all models that produce better SOC estimations on the same data set.

Lastly, the significant variance between different battery cells means that the results partly depend on the properties of the cell and do not necessarily transfer to other similar chemistries or even cells with the same chemistry. Furthermore, the fraction of silicon doping in the negative electrode affects the magnitude of the hysteresis effect on the terminal voltage, but in the tested cell the fraction is unknown as the manufacturer does not present this information in their datasheet.

7-2 Recommendations

Firstly, the RC-H and A-RC-H models both showed a lack of robustness to the initial SOC error. However, it is not clear whether a 20% initial SOC error will ever occur in a practical scenario or whether the tuned initial uncertainty is a good representation of the actual uncertainty. Typical initial SOC errors could be characterized using additional experiments to test the accuracy of SOC initialization methods, as described in Chapter 5. These experiments could validate the use of better initial SOC guesses and lower initial SOC uncertainties, which will improve the performance of the JUKF SOC estimation.

Secondly, it was shown that the SOC estimation error increases as the cell ages, likely due to drift in the SOC-OCV relationship. The estimation error might be improved by retuning the Kalman filter, but this is generally not viable in practical operations. Instead, one could investigate the use of adaptive Kalman filters that automatically retune the Q and R matrices, to improve long-term SOC estimation performance.

Thirdly, the models were limited to single RC-pair equivalent circuits. However, double RC-pair models are also commonly used and it would be interesting to compare the RC-H model with a double RC model on the same data set. These methods have similar complexity, as both add three joint state variables and one differential equation to the basic RC model.

Fourthly, the JUKF framework produces state and parameter estimates with one joint state vector at each time step, which is relatively computationally expensive. However, computational costs can be brought down by separating the joint filter into a state filter and a parameter filter. This Kalman filter decreases the size of the matrices and improves computational efficiency [43]. The complexity can be reduced further by recognizing that the states and parameters vary at different time scales. SOC, for example, typically varies faster than the ohmic resistance. In this multi-rate filter, the state filter is executed every time stamp, but the parameter filter is run at a lower frequency.

Lastly, this report mainly focused on improving SOC accuracy for silicon-doped lithium-ion cells but the main motivation for this is to achieve better capacity estimation accuracy to be able to extend the battery's total lifetime. To confirm the hypothesis that higher SOC accuracy leads to improved capacity estimation accuracy, the RC and RC-H frameworks should be combined with SOC-based capacity estimation methods and compared using suitable data sets.

Bibliography

[1] G. L. Plett, *Battery Management Systems, Volume I: Battery Modeling.* Artech, 2015.

[2] A. Manthiram, "An outlook on lithium ion battery technology," *ACS Central Science*, vol. 3, no. 10, pp. 1063–1069, 2017.

[3] G. Zubi *et al.*, "The lithium-ion battery: State of the art and future perspectives," *Renewable and Sustainable Energy Reviews*, vol. 89, pp. 292–308, 2018.

[4] M. S. Ziegler and J. E. Trancik, "Re-examining rates of lithium-ion battery technology improvement and cost decline," *Energy Environ. Sci.*, vol. 14, pp. 1635–1651, 2021.

[5] Q. Wang, "Thermal runaway caused fire and explosion of lithium ion battery," *Journal of Power Sources*, vol. 208, pp. 210–224, 2012.

[6] X. Fe *et al.*, "Mitigating thermal runaway of lithium-ion batteries," *Joule*, vol. 4, no. 4, pp. 743–770, 2020.

[7] A. B. Botelho Junior *et al.*, "Cobalt recovery from li-ion battery recycling: A critical review," *Metals*, vol. 11, no. 12, p. 1999, 2021.

[8] Y. Hua *et al.*, "Toward sustainable reuse of retired lithium-ion batteries from electric vehicles," *Resources, Conservation and Recycling*, vol. 168, p. 105249, 2021.

[9] G. L. Plett, *Battery Management Systems, Volume II: Equivalent-Circuit Methods.* Artech, 2016.

[10] C. P. Graells *et al.*, "Differential hysteresis models for a silicon-anode li-ion battery cell," *IEEE Transportation Electrification Conference & Expo (ITEC)*, pp. 175–180, 2020.

[11] D. Wycisk *et al.*, "Modified plett-model for modeling voltage hysteresis in lithium-ion cells," *Journal of Energy Storage*, vol. 52, p. 105016, 2022.

[12] A. Farmann *et al.*, "Critical review of on-board capacity estimation techniques for lithium-ion batteries in electric and hybrid electric vehicles," *Journal of Power Sources*, vol. 281, pp. 114–130, 2015.

[13] R. Xiong *et al.*, "Towards a smarter battery management system: A critical review on battery state of health monitoring methods," *Journal of Power Sources*, vol. 405, pp. 18–29, 2018.

[14] Vlaamse Instelling voor Technologisch Onderzoek (VITO); Commissariat à l'Energie Atomique et aux Energies Alternatives (CEA); Siemens; Technische Universität München (TUM); TÜV SÜD Battery Testing and others, "Everlasting: Electric vehicle enhanced range, lifetime and safety through ingenious battery management. Version 11," *4TU.ResearchData. Collection*, 2021.

[15] J. Mitali *et al.*, "Energy storage systems: A review," *Energy Storage and Saving*, vol. 1, no. 3, pp. 166–216, 2022.

[16] H. Aral and A. Vecchio-Sadus, "Toxicity of lithium to humans and the environment—a literature review," *Ecotoxicology and Environmental Safety*, vol. 70, no. 3, pp. 349–356, 2008.

[17] L. Leyssens, "Cobalt toxicity in humans—a review of the potential sources and systemic health effects," *Toxicology*, vol. 387, pp. 43–56, 2017.

[18] X. Shen *et al.*, "Advanced electrode materials in lithium batteries: Retrospect and prospect," *Energy Mater Adv.*, vol. 2021, 2021.

[19] H. Ryu *et al.*, "Reducing cobalt from lithium-ion batteries for the electric vehicle era," *Energy Environ. Sci.*, vol. 14, p. 844, 2021.

[20] Y. Huang *et al.*, "Lithium manganese spinel cathodes for lithium-ion batteries," *Advanced Energy Materials*, vol. 11, no. 2, p. 2000997, 2021.

[21] H. Zhang *et al.*, "Graphite as anode materials: Fundamental mechanism, recent progress and advances," *Energy Storage Materials*, vol. 36, pp. 147–170, 2021.

[22] X. Zhang *et al.*, "Hybrid lithium iron phosphate battery and lithium titanate battery systems for electric buses," *IEEE Transactions on Vehicular Technology*, vol. 67, no. 2, pp. 956–965, 2018.

[23] S. S. Madani *et al.*, "An electrical equivalent circuit model of a lithium titanate oxide battery," *Batteries*, vol. 5, no. 1, p. 31, 2019.

[24] Z. Liu *et al.*, "Safer lithium-ion batteries from the separator aspect: Development and future perspectives," *Energy & Environmental Materials*, vol. 4, no. 3, pp. 336–362, 2021.

[25] X. Han *et al.*, "A review on the key issues of the lithium ion battery degradation among the whole life cycle," *ETransportation*, vol. 1, p. 100005, 2019.

[26] C. R. Birkl *et al.*, "Degradation diagnostics for lithium ion cells," *Journal of Power Sources*, vol. 341, pp. 373–386, 2017.

[27] J. Vetter *et al.*, "Ageing mechanisms in lithium-ion batteries," *Journal of Power Sources*, vol. 147, no. 1-2, pp. 269–281, 2005.

[28] C. Zhan *et al.*, "Mn(ii) deposition on anodes and its effects on capacity fade in spinel lithium manganate–carbon systems," *Nat. Commun.*, vol. 4, no. 2437, 2013.

[29] R. Hausbrand *et al.*, "Fundamental degradation mechanisms of layered oxide li-ion battery cathode materials: Methodology, insights and novel approaches," *Materials Science and Engineering: B*, vol. 192, pp. 3–25, 2015.

[30] J. Newman *et al.*, "Modeling of lithium-ion batteries," *Elsevier*, vol. 119-121, pp. 838–843, 2003.

[31] H. He *et al.*, "Evaluation of lithium-ion battery equivalent circuit models for state of charge estimation by an experimental approach," *Energies*, vol. 4, no. 4, pp. 582–598, 2011.

[32] C. Huang and M. Chow, "Accurate Thevenin's circuit-based battery model parameter identification," *IEEE 25th International Symposium on Industrial Electronics (ISIE)*, 2016.

[33] D. Andre *et al.*, "Characterization of high-power lithium-ion batteries by electrochemical impedance spectroscopy. ii: Modelling," *Journal of Power Sources*, vol. 196, no. 12, pp. 5349–5356, 2011.

[34] K. Movassagh *et al.*, "A critical look at Coulomb counting approach for state of charge estimation in batteries," *Energies*, vol. 14, no. 14, p. 4074, 2021.

[35] F. Yang *et al.*, "A study of the relationship between coulombic efficiency and capacity degradation of commercial lithium-ion batteries," *Energy*, vol. 145, pp. 486–495, 2018.

[36] F. Zheng *et al.*, "Influence of different open circuit voltage tests on state of charge online estimation for lithium-ion batteries," *Applied Energy*, vol. 183, pp. 513–525, 2016.

[37] A. Barai *et al.*, "A study of the open circuit voltage characterization technique and hysteresis assessment of lithium-ion cells," *Journal of Power Sources*, vol. 295, pp. 99–107, 2015.

[38] B. Pattipati, "Open circuit voltage characterization of lithium-ion batteries," *Journal of Power Sources*, vol. 269, pp. 317–333, 2014.

[39] P. Pillai *et al.*, "Open-circuit voltage models for battery management systems: A review," *Energies*, vol. 15, no. 18, p. 6803, 2022.

[40] E. A. Wan and R. Van Der Merwe, "The unscented kalman filter for nonlinear estimation," *Proceedings of the IEEE 2000 Adaptive Systems for Signal Processing, Communications, and Control Symposium (Cat. No.00EX373), Lake Louise, AB, Canada*, pp. 153–158, 2000.

[41] R. Van der Merwe and E. A. Wan, "The square-root unscented Kalman filter for state and parameter-estimation," *IEEE International Conference on Acoustics, Speech, and Signal Processing*, vol. 6, pp. 3461–3464, 2001.

[42] H. M. T. Menegaz *et al.*, "A systematization of the unscented Kalman filter theory," *IEEE Transactions on Automatic Control*, vol. 60, no. 10, pp. 2583–2598, 2015.

[43] G. L. Plett, "Extended kalman filtering for battery management systems of lipb-based hev battery packs: Part 3. state and parameter estimation," *Journal of Power Sources*, vol. 134, no. 2, pp. 277–292, 2004.

List of Abbreviations

A-RC-H	Adaptive OCV with Resistor Capacitor Pair and Hysteresis
BOL	Begin-of-life
CC-CV	Constant current, constant voltage
CEI	Cathode-electrolyte interphase
CPE	Constant phase element
DCT	Driving cycle test
DST	Dynamic stress test
EKF	Extended Kalman filter
EOL	End-of-life
EV	Electric vehicle
JUKF	Joint unscented Kalman filter
LAM	Loss of active material
LCO	Lithium cobalt oxide
LFP	Lithium iron phosphate
LLI	Loss of lithium inventory
LMO	Lithium manganese oxide
LTO	Lithium titanate oxide
MAE	Mean-absolute error
MAXAE	Maximum-absolute error
NCA	Nickel cobalt aluminum
NMC	Nickel manganese cobalt
OCV	Open-circuit voltage
OLS	Ordinary least squares
RC	Resistor Capacitor Pair
RC-H	Resistor Capacitor Pair and Hysteresis
RMSE	Root-mean-square error
SEI	Solid-electrolyte interphase
Si-C	Silicon-doped graphite
SOC	State-of-charge
SOH	State-of-health
SR-UKF	Square-root unscented Kalman filter
UKF	Unscented Kalman filter
UT	Unscented transform